Chapter 4. Post-subduction, alkaline volcanism – Petrology & Petrogenesis

Hole, M.J.[1]

[1]*Department of Geology & Petroleum Geology, University of Aberdeen, AB24 3UE, UK*

Abstract.

Scattered occurrences of Miocene-Recent volcanic rocks of the alkaline intraplate association represent one of the last expressions of magmatism along the Antarctic Peninsula. The volcanic rocks were erupted after the cessation of subduction which stopped following a series of northward-younging ridge-crest–trench collisions. Volcanism has been linked to the development of a growing slab window beneath the extinct convergent margin. Geochemically, lavas range from olivine tholeiite through to basanite and tephrite. Previous studies have emphasized the slab window tectonic setting as key to allowing melting of peridotite in the asthenospheric void caused by the passage of the slab beneath the locus of volcanism. This hypothesis is revisited in the light of more recent petrological research, and an origin from melting of subducted slab-hosted pyroxenite is considered here to be a more viable alternative for their petrogenesis. Because of the simple geometry of ridge subduction, and the well-established chronology of ridge-crest-trench collisions, the Antarctic Peninsula remains a key region for understanding the transition from active to passive margin resulting from cessation of subduction. However, there are still some key issues relating to their tectono-magmatic association, and principally, the poor geochronological control on the volcanic rocks requires urgent attention.

Distribution of the volcanic rocks and their tectonic setting

Scattered along the length of the Antarctic Peninsula are exposures of Miocene–Recent volcanic rocks of the intraplate alkaline association (Fig, 1; Smellie 1987; Hole 1988; Hole 1990*a, b, c*; Hole & Thompson 1990; Hole et al 1991; 1993; 1994a; Hole & Larter 1993; Hole & Saunders 1996). Whereas these occurrences are limited in volume they have great significance because they were erupted after, or nearly synchronous with the cessation of more than 200 Ma of easterly-directed subduction along the Antarctic Peninsula and the formation of slab windows. Subduction ceased because of north easterly–younging collisions between ridge crests of the Antarctic Phoenix spreading centre and the continental margin, which ultimately resulted in the transformation of the margin from active and convergent to passive. The complex interactions between ridge-crests and the trench along the Antarctic Peninsula from 55 Ma until the present have been summarized and illustrated by the animations included in Eagles *et al.* (2007).

Chapter 4. Post-subduction, alkaline volcanism – Petrology & Petrogenesis

Ridge-crest–trench collisions occurred between ~50Ma off the coast of Alexander Island and ~3.1 at the 'C' Fracture Zone (Figs 2-4). At the locus of each collision a ridge-crest–trench–transform triple junction formed and subduction stopped at the same time as each collision. The trailing flank of the ridge crest was not subducted and the subducted slab in the collision zone remained attached to the slab to the northeast *via* an adjacent fracture zone. Thus, to the northeast of each triple junction, the slab continued to sink into the asthenosphere because of continued subduction to the northeast. This ultimately resulted in the formation of a slab window. Each collision event destroyed a segment of the Phoenix Plate, such that the continental crust of the Antarctic Peninsula and the sea-floor to the west were all part of the Antarctic Plate and consequently represent a passive margin. In the youngest two collision zones, between the North Anvers and Hero Fracture Zones, there was a slight complication to this simple scenario. The pattern of magnetic anomalies suggests that, starting about 9 Myr ago, development of a deformation zone between the "C" and Hero fracture zones partially de-coupled the part of the leading plate to the southwest from the leading plate to the northeast. Spreading and subduction continued to the southwest of the deformation zone, albeit more slowly than to the northeast, until the whole of both ridge crest segments between the North Anvers and Hero Fracture Zones had collided with the margin (Larter & Barker, 1991). At the South Shetland Islands Trench, subduction activity decreased sharply after 6 Ma and stopped or became very slow after the cessation of spreading in Drake Passage at about 3.3 Ma (Jin et al. 2009). Choe et al. (2007) showed that fossilized Antarctic-Phoenix Ridge segments occur offshore of the South Shetland Islands and consist of older N-MORB (3.5-6.4 Ma) formed prior to the extinction of spreading and younger E-MORB (1.3-3.4 Ma) formed after extinction. Thus, the South Shetlands Island Trench is the only part of the Antarctic Peninsula that retains any vestige of post-Miocene subduction. Here, a summary will be provided of the ridge-crest interactions along the Antarctic Peninsula which are directly related to the Miocene to Recent volcanism.

The concept of slab windows in relation to the subduction of triple junctions was first developed by Dickinson and Snyder (1979), and their model predicted that the for situations where there is near parallelism of ridge crest segments with the subduction trench should result in the formation of "zig-zag"–shaped window increasing in width to the from the oldest to youngest collision events. This is what tectonic reconstructions for the Antarctic Peninsula suggest (Fig. 2). The geometry of slab windows is consequently dependent on the convergence angle of the relevant ridge crest; oblique collision results in triangular slab windows whereas nearly orthogonal collision of a segmented length of ridge crest forms of a "zig-zag" shaped slab window (Dickinson & Snyder, 1979). This hypothesis was developed for the Pacific margin of

the Americas (e.g. Storey et al. 1989; Thorkelson & Taylor 1989; Hole et al. 1991; Thorkelson 1996; Johnson & Thorkelson 2000; D'Orazio et al. 2001; Thorkelson & Breitsprecher 2004; Breitsprecher & Thorkelson 2009; Thorkelson et al 2011) demonstrating that the entire region had been underlain by slab windows during various periods throughout the Cenozoic. Consequently, the Antarctic Peninsula is not unique in displaying a relationship between ridge-crest–trench collisions and alkaline magmatism but is certainly the best constrained in terms of the seafloor magnetics data set and accuracy of tectonic reconstructions (e.g. Barker 1982; Eagles et al. 2007).

Figure 4 which is adapted from Hole et al. (1994*a*), illustrates the width of individual slab window segments projected onto the horizontal surface of the continental crust from 15 Ma to the present in relation to the geographical distribution of post-subduction alkalic basalts. Note that some of the collision events were slightly oblique but for the sake of clarity and ease of calculation we have assumed that all collisions were orthogonal. The x-axis represents the palaeo-trench and the different ornaments correspond to the amount of slab window formation associated with each spreading ridge, the solid lines separating the ornaments being "isochrons" for the slab window formation. The assumptions that are used in the calculations are that the angle of slab dip was 45°, and the rate of opening of an individual slab window segment was dependent on the spreading rate of the adjacent ridge crest to the north (Barker, 1982; Larter & Barker, 1991). It is also assumed that the subducted slab was planar, and the slab dip did not vary over time. Reducing the slab dip to 30° increases the linear width scale from 0 to 400 km to 0 to 500 km. The rate of slab window opening is not constant because spreading took place about a near pole to the southwest and spreading rates varied with time. These figures clearly show that trench proximal volcanic rocks from Dredge 138 overlie the C fracture zone, where a slab window to the south began to open at around 6.0 Ma. However, the relationship between the timing of slab window formation and the earliest eruptions in each sector is not simple and there is no clear south—north age progression, a feature not yet satisfactorily explained (cf. Larter & Barker 1991; Hole 1988; Hole et al. 1994*a*).

The three largest occurrences of post-subduction basalts in the region are exposed on Alexander Island, Seal Nunataks and James Ross Island (Fig. 1). The landward extrapolation of three fracture zones in the northern part of the Antarctic Peninsula (N Anvers, S Anvers and C; Figs 3 and 4) are oriented sub-parallel to the exposures of alkalic basalts at Seal Nunataks, to the rear of the palaeo-arc, and this has been causally linked to post-subduction volcanism. (Hole 1990). Post-subduction volcanism on Alexander Island post-dates ridge-crest–trench collision by more than 40 Ma (Hole 1988). At James Ross Island the relationship between the likely

development of a slab window and volcanism is complicated by the existence of the Bransfield Strait marginal basin to the west and the continued subduction, albeit very slow, at the South Shetland Islands.

Post-subduction magmatism comprises two sodic alkaline magmatic series characterised by basanites—phonotephrites and alkali basalts—tholeiites (Smellie, 1987; Hole et al., 1994a). As a result, a series of extensive monogenetic volcanic fields and small isolated centres were created, scattered along the length of the Antarctic Peninsula, between Seal Nunataks in the north and Snow Nunataks in the south (Smellie et al. 1988; Smellie 1999; Fig. 1). The outcrops include a variety of volcanic landforms including scoria cones, tuff cones and tuyas, and some outcrops are dominated by dykes. The eruptive environments varied from subaerial to subglacial.

Petrology, Geochemistry and Petrogenesis

Petrographical and geochemical characteristics of the post-subduction volcanic rocks.

Representative analyses of lavas are given in Table 1. The total alkalis silica diagram (Le Bas & Strekheisen 1991) has been used to name each analysed sample in the region (Fig. 5). Evolved rocks with >52.5 wt% SiO_2 are not represented at all in the post-subduction suite. At northern Alexander Island (Fig 1), isolated, limited occurrences of volcanic rocks are single flow fields and associated volcaniclastic rocks and are silica-undersaturated (Fig. 6) basanites and tephrites with rare occurrences of hawaiite and mugearite. The subglacial pillow basalts and hyaloclastite sequences of Beethoven Peninsula are mostly alkali basalt with rare hawaiite at Gluck Peak. Volcanic rocks at James Ross Island are mostly alkali basalt with limited occurrences of hawaiite. At Seal Nunataks (Fig. 1) alkali basalt, subalkalic basalt and basaltic andesite are all represented. On a CIPW-normative tetrahedron (Thompson 1982) the post-subduction basalts span Si-undersaturated, Ne-normative alkali olivine basalts to Si-saturated, *Hy*-normative olivine tholeiites, with data some Seal Nunataks samples falling on the *Di–Hy* join and approaching Si-oversaturation (Fig. 6). Notably, the *Hy*-normative olivine tholeiites are most abundant at Seal Nunataks and Beethoven Peninsula, whereas occurrences in northern Alexander Island are predominantly *Ne*-normative compositions. Also included in Figs 5 & 6 are data for ~9 Ma volcanic rocks from the Jones Mountains 750km WSW of Alexander Island (Hole et al. 1993b). Whereas these are not specifically part of the Antarctic Peninsula post-subduction volcanic province, they have strong geochemical affinities with lavas from Seal Nunataks and do not appear to be part of the Marie Byrd Land Province farther to the south (Hole et al. 1993b; Hole & LeMasurier 1994).

Fine-grained to near-glassy olivine-phyric basalts are the most common petrographic type. Most olivine phenocrysts are euhedral and may be skeletal suggesting crystallization from the melt rather than accumulation. Plagioclase phenocrysts are rare but are developed in some hawaiites from Beethoven Peninsula and basaltic andesites from Seal Nunataks. Augite is very rare and is restricted to alkali olivine basalts at Seal Nunataks and occurs in a variolitic texture within the glassy groundmass of the lavas. For Seal Nunataks samples with MgO in the range 7.0-8.6 wt%, olivine varies from Fo74.4-84.3 although olivine phenocrysts are generally not in equilibrium with the whole-rock and olivine has lower Fo than would be expected for the Mg# of the whole rock for $K_{D[Fe\text{-}Mg]}^{Ol/L}$=0.30 and FeO/FeO_T=0.9 (Putirka 2008). This is best explained by the accumulation of olivine in the most MgO-rich samples, although the volume of olivine accumulation is small. For example, for sample R.3717.1 (8.6 wt% MgO) removal of 10% olivine of the observed phenocryst composition (Fo78) would be needed to provide olivine-liquid equilibrium, and for other Seal Nunataks samples, this amount of olivine would be less.

Selected major elements plotted against MgO wt% are shown in Fig. 7. Covariations between Al_2O_3 and MgO (Fig. 7) clearly demonstrates that most of the post-subduction volcanic rocks are related to the olivine liquidus and there is no major role for plagioclase in their crystallization histories because plagioclase strongly fractionates Al_2O_3 relative to MgO resulting in positive covariations between the two oxides for rocks that have crystallizaed plagioclase. A Petrolog3 (Danyuchevsky & Plechov 2011) forward crystallization model for the highest MgO, but nevertheless olivine-poor sample from Seal Nunataks (R.3719.1; 11 wt% MgO) shows that plagioclase is predicted to join olivine on the liquidus at ~7.5 wt% MgO which is well within the range for olivine tholeiitic compositions from the ocean basins (Hole 2018). Two trends are evident on the SiO_2 *versus* MgO diagram. James Ross Island lavas represent a low SiO_2 (maximum 50wt% SiO_2) series of lavas which is also followed by lavas from northern Alexander Island. A higher SiO_2 trend (up to 52.5 wt% SiO_2) characterizes some lavas from Seal Nunataks, those from southern Alexander Island and those from dredge site 138. A small number of Seal Nunataks lavas fall on the lower SiO_2 trend. This is evident also in the CIPW normative tetrahedron and data for the low SiO_2 lavas from Seal Nunataks lavas falls close to the Ol–Di join, and data for the high SiO_2 lavas scatters across the Ol–Hy–Di plane of the projection. Lavas on the high SiO_2 trend have similar distributions of MgO and SiO_2 to N-MORB from the East Pacific Rise (Fig. 7a). All the post-subduction lavas are notably deficient in CaO for a given MgO content (Fig. 7d) compared to MORB. Whereas CaO depletion can be the result of crystallization of augite at elevated pressures (Hole 2018) this is unlikely to be the case for the post-subduction basalts because they follow olivine control lines in terms of MgO-Al_2O_3

variations, and augite is rare in the lavas. Additionally, the cotectic for crystallization at ~0.9 GPa results in a vector in the opposite direction from crystallization at near-surface pressure in the CIPW normative tetrahedron (Fig. 6) and Seal Nunataks lavas exhibit decreasing MgO content away from the olivine apex and towards the Di–Hy join. Consequently, the low CaO contents must be a characteristic that was inherited from their mantle source-region. Lavas from northern Alexander Island exhibit a positive correlation between MgO and TiO_2 and have consistently higher TiO_2 for a given MgO than any other of the post-subduction lavas (Fig. 7b). Lavas from the remaining localities exhibit a broadly negative MgO-TiO_2 covariation. Ni (30-250 ppm) and Cr (50-400ppm) behave compatibly during crystallization of the post-subduction lavas and exhibit positive linear covariations between Ni, Cr and MgO.

The incompatible trace element characteristics of the post-subduction lavas are shown in Fig. 8 as a series of profiles normalized to primitive mantle (Sun & McDonough 1989). All samples have incompatible trace element profiles typical of 'within plate' alkali basalts and such patterns can be found in many oceanic island 'hotspot' basalts (OIB) as well as continental alkali basalts (e.g. Hole & LeMasurier 1994). E-MORB from the Antarctic Phoenix Ridge (Choi et al. 2007) exhibit similar trace element profiles to Seal Nunataks samples. All the profiles peak at elements Nb and Ta and are light rare earth element (LREE) enriched LREE-enrichment and have low absolute concentrations of Sc (18-25 ppm) and Y (17-25 ppm) characteristics that are all consistent with melting of a mantle source leaving residual garnet with which the heavy rare earth elements (HREE), Sc and Y are compatible. Northern Alexander Island basanites exhibit the greatest LREE-enrichment and highest Nb/Zr ($[La/Yb]_N$ ~19.5; Nb/Zr ~0.27 for Rothschild Island basanite) and Seal Nunataks Hy-normative olivine tholeiites the lowest $[La/Yb]_N$ Nb/Zr (~5.3 and ~0.12 for Christensen Nunatak). James Ross Island samples exhibit an almost complete overlap with Seal Nunataks samples in Fig. 8. Trench proximal alkali basalts (Fig. 2; Hole & Larter 1993) similarly fall within the range for Seal Nunataks and overlap in composition with E-MORB produced at the Antarctic-Phoenix Ridge. Significantly, there is no vestige of a subduction component in any of the basalts; Th/Ta (0.9-1.5), La/Nb (0.7-1.2) are within the expected ranges for lavas erupted distant in space and time from subduction zones.

The lavas exhibit a restricted range of isotopic compositions (Fig. 9) and differ from N-MORB from the Pacific Ocean in having lower $^{143}Nd/^{144}Nd$ (0.51278–0.51300) for a given $^{87}Sr/^{86}Sr$ (0.7025-0.7040) than N-MORB, and more radiogenic $^{206}Pb/^{204}Pb$ and $^{207}Pb/^{204}Pb$ than N-MORB. The post-subduction basalts have similar Sr- and Nd- isotopic compositions to so-called HIMU OIB but a HIMU source is precluded because none of the post-subduction lavas possess the high $^{206}Pb/^{204}Pb$ (>20) that characterizes HIMU OIB (e.g. Palacz & Saunders 1986;

Homrighausen et al. 2018). Whereas some of the samples from James Ross Island and Seal Nunataks with $^{87}Sr/^{86}Sr$ ~0.7034 may have undergone limited interaction with sialic upper crust (Hole et al. 1993), they could equally be a feature of the mantle source from which the basalts were derived. In support of the former, glassy 'buchite' xenoliths representing partially melted arkosic sediments occur at Seal Nunataks, James Ross Island and Beethoven Peninsula, but the lack of a trace element signature of such interaction supports the former. Since the available arkosic sedimentary rocks in the area are likely to be Cretaceous back-arc sedimentary rocks, and these were all derived from the Antarctic Peninsula convergent margin, a subduction signature in the trace element compositions of the alkali basalts might be an expected result of crustal contamination, but this is not seen. As with the trace element profiles discussed above, there is a strong similarity between the isotopic compositions of E-MORB being erupted at the Antarctic Phoenix Ridge and the post-subduction lavas.

Petrogenesis and relationship to slab window formation.

The lack of any subduction signature in the post-subduction basalts means that the normal subduction related melting regime involving dehydration melting of the mantle wedge must have ceased before their generation. Therefore, the source of the post-subduction alkali basalts cannot have been from mantle that had been involved in the subduction process. This implies that sub-slab mantle may have been involved in magma genesis (Hole 1990; Hole et al 1993) or that the entire mantle wedge was replenished with pristine peridotite immediately after subduction stopped. In terms of P-T conditions, generation of the observed LREE-enrichment would require all melting to occur at >2.7 GPa (Fig. 10a) since this is the minimum pressure at which garnet is a stable phase on the dry peridotite solidus. Since melt is produced by decompression melting, for initial intersection of the dry solidus at ~2.7 GPa melting would continue into the spinel stability field of mantle peridotite and the garnet signature in the REE would be rapidly lost. Consequently, to preserve the garnet melting signature, all melting would have to occur at pressures substantially >2.7 GPa. This means that the post-subduction basalts should have formed by melting at a mantle temperature that is much higher, and perhaps up to 1450°C, than that accepted for ambient temperature along continental margins.

The current published model for the generation of the post-subduction lavas requires upwelling of the asthenosphere to fill the incipient void left by the subducting slab after slab-window formation which promoted decompression melting and the ultimate eruption of the alkalic basalts (Hole, 1988; 1990; Hole & Larter 1993; Hole et al 1993; 1994a; D'Orazio et al. 2001). Alkalic basalts associated with slab-windows are not unique to the Antarctic Peninsula; similar volcanism occurs at San Quintín, Baja California, (Storey et al. 1989) in central southern

British Columbia (Bevier 1983; Thorkelson & Taylor 1989) and in Patagonia (e.g. D'Orazio et al. 2001; Breitspracher & Thorkelson 2009). It has been recognized that there are similarities in the trace element and isotopic compositions of the post-subduction lavas and OIB, and it is generally accepted that the latter are the result of melting at elevated mantle temperatures associated with mantle plumes originating at the core-mantle boundary. However, to produce the post-subduction lavas by this method would require the fortuitous and spontaneous initiation of plumes when subduction ceased; basic geological observations alone also encourage the hypothesis of a genetic link between slab-windows and alkalic magmatism (Hole et al 1991). Furthermore, most subduction-related magmatism is generally considered to occur at ambient T_P with magma generated along the H_2O-saturated peridotite solidus (e.g. Hacker et al 2003; Grove et al 2012) and so there is no reason why a higher than ambient T_P would be expected along the Antarctic Peninsula margin at the time subduction stopped.

If the mantle beneath the Antarctic Peninsula was at ambient T_P of 1350°C, the difficulty arises that the mantle adiabat does not intersect the dry peridotite solidus to generate melt until ~ 2 GPa which is within the spinel stability field of the upper-mantle; such a melting regime would not be capable of generating the observed LREE-enrichment in the basalts (Fig. 10a). Conversely, the MgO-SiO_2 covariations (Fig. 7), particularly for the high SiO_2 lineage in lavas at Seal Nunataks, and their similarity to N-MORB, is a common manifestation of shallow melting. High pressure melts formed with garnet on the peridotite are lower in SiO_2 for a given MgO than N-MORB. Herein lies the paradox. If it assumed T_P was ambient, then the apparent high-pressure signature in the REE and the apparent low-pressure signature in the major elements in the same lavas needs to be explained. D'Orazio et al. (2001) recognized the same paradox for the post-subduction alkali basalts of Patagonia and noted that LREE-enrichment required melting at ≥2.7 GPa but SiO_2 contents of up to 51.0 wt% at 8.5 wt% MgO, were more akin to those of shallow melting at <1.5 GPa. D'Orazio et al. (2001) therefore appealed to a process involving the mixing between shallow harzburgite–derived melt and deeper garnet-peridotite–derived melt to account for this unusual geochemical trait. However, such a model is still unable to account for the intersection of the dry solidus at > 2.7 GPa at ambient T_P of 1350°C.

Further constraints of the mantle temperature in the region can be gained from lavas erupted at the Antarctic Phoenix Ridge. The petrological modelling routine PRIMELT3 (Herzberg & Asimow 2008; 2015) allows estimates of T_P to be made using whole-rock data for lavas that have only fractionated olivine (Herzberg & Asimow 2015; Hole & Millett 2016). None of the post-subduction basalts yield useful temperature information using this method because all are too deficient in CaO at a given MgO content to have been derived from dry peridotite, which in itself

is a useful observation. Whole-rock data for the basalts from the 3.1-3.5 Ma Antarctic Phoenix Ridge also do not yield any useful temperature data because they crystallization along the L + Ol + Pl + Cpx cotectic (Choi et al. 2013). Melt inclusions trapped in olivine and plagioclase in Antarctic Phoenix Ridge N-MORB samples are less fractionated parcels of melt than their host whole-rock compositions. Using PRIMELT3, melt inclusions reveal T_P=1336±21°C (Appendix 1) a figure that is within the uncertainty of that determined for Siqueiros Fracture Zone MORB by the same method (Herzberg & Asimow 2015) and therefore within the temperature range for ambient mantle. This suggests that at ~3 Ma magma generation at the Antarctic-Phoenix Ridge was taking place at ambient mantle temperature. At this time, the slab window had already propagated as far as the Hero Fracture Zone (Fig.3) and any regional elevation in T_P would therefore be evident in the Antarctic-Phoenix Ridge basalts, which it is not. Indeed, another important observation is that different segments of the Antarctic-Phoenix Ridge produce either N-MORB or E-MORB and the latter is indistinguishable from the post-subduction basalts in terms of incompatible trace elements and isotopic compositions (Figs 8 & 9). Therefore, at the Antarctic-Phoenix Ridge, basalts with similar trace element and isotopic compositions to the post-subduction basalts were formed at ambient T_P. Therefore, the garnet melting signature of the basalts must be due to a factor other than elevated T_P.

Melting of volatile-bearing peridotite.

Hole & Saunders (1996) suggested that melting of volatile-enriched, high CO_2/H_2O peridotite, might be the solution to the paradox because the dry peridotite solidus is supressed by the addition of volatiles such that the mantle adiabat interests the volatile-bearing solidus at a higher pressure for a given temperature compared to the situation for dry peridotite (Fig. 10a). The presence of kaersutite megacrysts in some of the lavas was cited evidence for the possible hydrous nature of their mantle source region. However, at the time that this hypothesis was proposed there was little information on the detailed effect of small concentrations of volatiles on the melting behaviour of dry peridotite. More recently, Sarafian et al (2017) and Dasgupta et al. (2007; 2013) have performed melting experiments on peridotite in the presence of H_2O (200 and 450 ppm) and CO_2 (5-25 wt%). In both cases, the experiments were for volatile undersaturated conditions, which differs from the volatile-saturated conditions which occur during subduction-related magmatism. For peridotite plus 450 ppm H_2O, the highest experimentally determined H_2O content (Sarafian et al 2017) the 1350°C adiabat intersects the damp solidus at almost exactly 2.7 GPa and so this is considered and unlikely mechanism for melt generation along the Antarctic Peninsula because most melt would be generated in the presence of spinel not garnet.

Chapter 4. Post-subduction, alkaline volcanism – Petrology & Petrogenesis

Dasgupta et al. (2007; 2013) showed that for a pressure range of 2-5 GPa and for 5-25 wt% CO_2, the peridotite solidus is progressively suppressed to lower temperatures at a given pressure (Fig. 10a). For an ambient T_P of 1350°C and ~10 wt% CO_2, the adiabat would intersect the peridotite solidus at >2.7 GPa (Fig. 10a) and this can be considered to be the lower limit of CO_2 required to generate all melting in the presence of garnet. Herzberg & Asimow (2008; 2015) provide a simple plot of CaO *versus* SiO_2 which serves to discriminate between melt generated in the presence of varying concentrations of CO_2 and dry melting (Fig. 10b). Progressively increasing CO_2 content causes decreasing in SiO_2 and increasing in CaO compared to dry melting, which also means that melts formed in the presence of CO_2 tend to be strongly *Ne*-normative. However, none of the post-subduction lavas have CaO and SiO_2 contents that fall within the region reserved for CO_2-rich melting in Fig. 10b even though some are Ne-normative (Fig. 8). For comparison, Cenozoic volcanic rocks from the West Antarctic Rift System (WARS) Wörner et al. 1989; Martin et al. 2013) are shown in Fig. 10b, and WARS lavas with > 7.0 MgO are clearly identified as being related to melting in the presence of CO_2. Consequently, neither H_2O-present nor CO_2-present melting can generate lavas that carry a garnet signature and exhibit the observed SiO_2-CaO covariations.

A slab-hosted pyroxenite source for the alkali basalts.

It is well established that mantle peridotite is not the only source for alkali basalts (Herzberg 2006; 2011; Sobolev et al. 2005) and that the large volumes of olivine tholeiite produced at Hawaii were derived from pyroxenite lithologies within the upper-mantle. The pyroxenite that contributes to magmatism at Large Igneous Province (both oceanic and continental) is generally considered to have its origin in recycled subducted slabs that are later entrained in hot upwelling mantle plumes. On subduction, the transformation of basaltic crust produces quartz or coesite eclogite in the upper mantle and these are termed stage 1 pyroxenites (Herzberg 2011). Cumulates of dunite, troctolite and olivine gabbro will yield olivine pyroxenite lithologies (Ol+Cpx+Gt) in the upper mantle. Stage 1 pyroxenites can therefore be classified into two distinct lithologies; silica enriched (SE) relating to metamorphism and recycling of basaltic crust, and silica deficient (SD) relating to recycling of gabbro and other cumulate rocks (Herzberg 2011). Laboratory melting experiments performed on both SD and SE pyroxenite lithologies show that they can generate basaltic melt under a variety of P-T conditions (Lambart et al. 2009, 2012, 2013). Significant to the current discussion is that fact that pyroxenite is likely to melt at a lower temperature for a given pressure than mantle peridotite, such that for a given T_P the pyroxenite solidus is intersected deeper in the mantle than the peridotite solidus (Fig.11). However, Lambart et al. (2016) showed that the Na, K and Ti content of pyroxenite has a

profound effect on melting behaviour, and that some SiO_2 poor pyroxenite which is also low in total alkalis and TiO_2 may have very similar melting behaviour to mantle peridotite. In general, however, high-SiO_2, alkali-rich pyroxenites will melt at a higher pressure for a given T_P than low SiO_2, alkali poor pyroxenite. Garnet is stable on the pyroxenite solidus to much lower pressures than for peridotite (~1.7 GPa; Kogiso et al. 2003; Lambart et al. 2013) so regardless of the temperature of the mantle, a large proportion of the melting interval for pyroxenite is in the presence of garnet (Fig. 11) and additionally, melts derived from SE pyroxenite are SiO_2-rich (Herzberg 2011). Since the ancestral source of pyroxenite lithologies in the upper-mantle is subducted slabs and that pyroxenite melts can exhibit LREE-enrichment as well as silica-saturation, the possibility that the post-subduction lavas were derived from pyroxenite resident in the subducted slab is worthy of consideration.

Recognizing a pyroxenite contribution to magmatism

Distinguishing between peridotite and pyroxenite-derived melts and their related lavas is not a trivial problem. In the upper mantle both lithologies coexist and consequently magmas are generated which are hybrids from the two sources (e.g. Lambart 2017). Additionally, melting of some, particularly SD pyroxenite, can produce magmas that are indistinguishable from melts of peridotite (Hole 2018). Nevertheless, Herzberg & Asimow (2008) showed that at Hawaii, magmas derived by melting of pyroxenite were deficient in CaO for a given MgO content compared to peridotite-derived magmas. This is in part due to residual clinopyroxene in pyroxenite source that serves to produce a melting regime in which CaO is compatible (D_{CaO} >1). Fig. 12 shows the CaO and MgO distribution of the Seal Nunataks lavas alongside those for pyroxenite-derived magmas from Hawaii. Tholeiitic lavas from the Hawaiian Scientific Drilling Project (HSDP-2; Rhodes & Vollinger 2004) which are considered to have been derived almost entirely from pyroxenite all have lower CaO at a given MgO than peridotite derived magmas, and the peridotite-pyroxenite divide on the diagram is based on this data. Also shown are the positions occupied by near-primary magmas (Herzberg 2006; Sobolev et al. 2005) from Koolau recovered during KSDP (Koolau Scientific Drilling Project), and its Makapuu phase, which are the most extreme examples of pure, near-primary SE pyroxenite melts. Since olivine fractionation produced vectors subparallel to the pyroxenite-peridotite divide, the data for the Seal Nunataks lavas shown in Fig. 12 clearly have major element compositions that are more deficient in CaO at a given MgO than many Hawaiian SE pyroxenite derived melts. As discussed earlier, the CaO deficiency in the post-subduction lavas must have been inherited from their source because low pressure crystallization of olivine does not fractionate MgO relative to CaO. Fig. 12b shows covariations between SiO_2 and MgO for the same samples as in Fig. 12a. There

are clear similarities between the low SiO_2 and high SiO_2 lineages, representing the products of melting of SD and SE pyroxenite respectively (Herzberg 2006) found in the HSDP-2 drill core and those found in the Antarctic Peninsula post-subduction lavas.

Primary or very primitive melts derived from SE pyroxenite (basaltic crust) are recognized because they plot on the SiO_2-rich side of the orthopyroxene-calcium Tschermaks component (Opx-CaTs) join in the molecular projection of the system olivine–orthopyroxene–CaTs–silica (Fig. 13). Conversely, melts derived from SD pyroxenite (cumulates) plot to the SiO_2-poor side of the same plane. Since the Opx–CaTs join is a thermal divide at pressures associated with mantle melting i.e. > ~1.7 GPa (Kogiso et al. 2004; Herzberg 2011; Lambart et al. 2013) derivative magmas from the melting of high and low SiO_2 pyroxenite have divergent fractionation histories. At near melting pressures, low SiO_2 pyroxenite may undergo mixing with melts of mantle peridotite to form hybrid magmas, whereas melt derived from high SiO_2 pyroxenite cannot (Sobolev et al. 2005; Herzberg, 2011; Lambart 2017). Herzberg (2011) provides a method of calculating the composition of parental or near primary melts from lavas that have only fractionated olivine which is the method used here. The CMAS molecular projection (diopside-garnet-enstatite) is pressure sensitive, and so an estimate of pressure of melting can be determined from this diagram assuming olivine is the sole fractionating phase in a melt (Fig. 13b). Once the pressure of melting is determined, the liquid can then be projected along an olivine control line until it intersects the cotectic in the system Ol–CaTs–Qz (Fig. 13a) at the pre-determined pressure from the CMAS projection. Data for the Seal Nunataks lavas best lends itself to this type of petrological manipulation because there are sufficient data to determine that the lavas are related by olivine crystallization and it is these lavas that have been used here. The CMAS diagram yields a pressure of melting of ~2.5-3.0 GPa and olivine addition in the Ol–CaTs–Qz projection reveals a near-primary magmas close to the eutectic at 2.5-3.0 GPa. Most of the model primary magmas are related to an SD parent but some are related to an SE parent (Fig. 13; Table 2) which is consistent with the two lineages of lavas in the MgO-SiO_2 diagram (Fig. 12). The important information that this gives us is that the Seal Nunataks lavas could be related by olivine fractionation along to a 2.5-3.0 GPa eutectic in equilibrium with Cpx+Gt±Opx±Ol, that is, SD or SE pyroxenite.

Pyroxenite melting behaviour

The melting behaviour of pyroxenite compared to peridotite is shown in Fig. 11 and has been determined using the Melt-PX routine of Lambart et al (2016). The pyroxenite starting compositions have been chosen to represent both SD (M7-16) and SE (ID-16) pyroxenites formed by prograde metamorphism of cumulates and basaltic crust respectively. For both

samples there are compositional data from experimentally generated melts (Johnson & Draper, 1992; Lambart et al. 2009; 2012; 2016). For a 100% pyroxenite as the source lithology at T_P=1350°C, melting would commence at ~3.0 GPa for both SD and SE pyroxenites and garnet would be stable on the pyroxenite solidus. Because M7-16 and ID-16 have similar K_2O, Na_2O and TiO_2 contents, their melting behaviour and melt productivity rates are very similar (Fig. 11). The melt productivity of pyroxenite is much greater than that of peridotite at the same T_P (Fig. 11) and the ability to produce a large range in extents of melting, and importantly, melts which span a wide range of normative compositions, is available for pyroxenite melting. In Fig. 6 the normative composition of experimental melts of SD pyroxenite (Keshav et al. 2004) are shown, and as expected, the extent of melting increases with increasing temperature, but also melts become less Ne-normative and cross into the Ol–Di–Hy plane at moderate extents of melting. Therefore, melting of subducted slab-derived pyroxenite could explain the major element compositions of the post-subduction lavas without having to appeal to elevated mantle temperatures and/or 'damp' and/or CO_2 present melting. Additionally, the two distinct lineages present in the SiO_2 *versus* MgO diagram (Figs 9a and 12) can be explained by melting of SD (low SiO_2) and SE (high SiO_2) pyroxenite both of which would be resident in the remnant subducted oceanic crust. This also explains the paradox identified by D'Orazio et al. (2001) that required garnet-present melting at high pressures to explain REE distributions in the lavas, but low pressures of melting to explain the high SiO_2 *of the same lavas*, at the locus of the slab window in Patagonia.

Using the methods outlined in Lambart (2017) the composition of accumulated fractional melts generated by melting of basaltic ocean crust have been calculated. For bulk distribution coefficients for trace elements we have used the data of Pertermann & Hirschamm (2003) and Pertermann et al. (2004), and we have assumed a pyroxenite that is close mineralogically to eclogite, containing 25% Opx, 50% Cpx and 25% garnet (Pertermann & Hirschann 2003). The relationship between pressure of melting and melt productivity has been derived from Melt-PX, such that for decompression melting of eclogite at 1350°C the melt productivity coefficient is constrained (Fig. 11). For a 'typical' oceanic crust composition, the data of Lambart (2017) has been used. The results of the modelling are shown in Fig. 14. As can be seen, using this method we can reproduce all the trace element characteristics of the post-subduction basalts for melting over a pressure interval of 2.8-1.0 GPa and for 5-25% melting and the similarities with SE pyroxenite-derived tholeiite SR0125-6.25 from Mauna Loa (Rhodes & Vollinger 2004) are clear. Similarly, the composition of the post-subduction alkali basalts from Esperancia Glencross (D'Orazio et al. 2001) are also consistent with such a model (Fig. 8) and the Qz-normative

compositions found at that location most likely represent large extents of melting coupled with crystallization along the L+Opx+Cpx cotectic at low pressures.

The similarity between the E-MORB and the post-subduction lavas requires some further attention. The role of pyroxenite in the petrogenesis of MORB has been investigated by Lambart et al. (2009) and they noted that because of their higher melt productivities and lower solidus temperatures, 5% of pyroxenite in the source region may contribute up to 40% of the total melt production at otherwise 'normal' spreading ridges. The key to the contribution of pyroxenite to melting at spreading ridges is the complex solid–solid, liquid–liquid and solid–liquid reactions which take place between decompressing peridotite and pyroxenite (Herzberg 2011). The loss of one component i.e. peridotite melt, would dramatically reduce melt productivity of the remaining one i.e. pyroxenite. However, recognizing this contribution from pyroxenite is problematical because of the overwhelming influence of peridotite melting at spreading ridges (Lambart et al. 2009). Choe et al. (2007) showed that the fossilized Antarctic-Phoenix Ridge segments offshore of the south Shetland Islands consist of older N-MORB formed prior to the extinction of spreading and younger E-MORB after extinction. The older N-MORB (3.5-6.4 Ma) occur in the south-eastern flank of one segment and younger E-MORB (1.4-3.1 Ma) comprise a huge seamount at the former ridge axis of a different segment and a large volcanic edifice at the north-western flank of the same segment. They reasoned that the E-MORB were formed by melting of enriched veins in the heterogeneous sub-ridge mantle, and when spreading stopped, it was these veins that provided most of the melt. Here, we suggest that the E-MORB are local melts of pyroxenite, and when spreading stopped, the capacity for melt production by passive upwelling of peridotite melt was reduced and the predominant melt production was from pyroxenite which was already resident in oceanic crust. Upon subduction of half the spreading ridge, the rapid increase in pressure prevented further melting of this young, hot, pyroxenite until it reached P-T conditions above its solidus, which it would not do until it reached ~3.5 GPa or ~100 km (Fig. 11). Using the subduction model for warm, young slab of Hacker et al (2003) this could be achieved ~300-400 km from the palaeo-trench which in the Antarctic Peninsula would be the location of Seal Nunataks, for example.

Thermal structure before and after slab window formation.

Figure 15 illustrates a possible thermal scenario beneath the Antarctic Peninsula at the instant of ridge-crest−trench collision (Fig. 15a) and at the time of passage of the subducted half-ridge beneath Seal Nunataks (Fig. 15b). At the instant of ridge-crest−trench collision, subduction-related magmatism might still be active. However, the subducted slab at ~100km depth would

be ~28 million years old (Barker 1982) and whether the relatively young age of the subducted slab effected magma production rate compared to the earlier history of the Antarctic Peninsula is a subject of conjecture. However, it is possible that more limited alteration to serpentinite in young oceanic crust compared with older oceanic crust may have reduced the flux of volatiles into the mantle wedge (e.g. Grove et al. 2012). At this time, the temperature structure beneath the subducted slab is such that the solidus of pyroxenite M7-16 is not intersected and slab melting cannot take place. A few million years after ridge-crest–trench collision the thermal structure below the palaeo-trench is the same as at the time of collision (Fig. 15b). Continued subduction of the half spreading-ridge occurred and therefore the temperature gradient in the mantle beneath the subducted slab must change from the syn-subduction case to that approaching mantle with T_P= 1350°C. This thermal re-equilibration would also be aided by the upwelling of asthenosphere to fill the void formed by the passage of the subducted oceanic lithosphere (Hole & Saunders 1996). For T_P=1350°C the dry solidus for pyroxenite M7-16 would be intersected at 3.5 GPa and 1390°C producing melt and for this to occur the 1390°C geotherm must be at <3.5 GPa (Fig. 15b). Because the slab remnant continues to subduct due to its coupling to the active subduction zone north of the N Anvers Fracture Zone (Figs 3 & 4), melting will cease when the slab descends to a depth of ~120 km equivalent to 3.5 GPa because the pyroxenite will now be sub-solidus. Therefore, amount of melt that can be generated will be self-limiting, perhaps explaining the short period of post-subduction alkaline magmatism. The lack of a subduction signature in any of the slab window related basalts means that melt cannot have been produced from a source that was volatile-enriched during the previous subduction history of the arc. Whereas this thermal regime is appropriate to the tectonic setting of the Antarctic Peninsula, it would not apply in regions where slab windows formed during oblique ridge crest trench collisions as will be discussed below.

Hydrous and anhydrous subducted slabs and their relationship to magmatism

Slab window-related basalts are not always of the intraplate alkaline association. Thorkelson & Breitsprecher (2004) noted that adakitic magmas, many of which can be classified as high MgO andesites (e.g. Storey et al. 1989), form by partial melting of 'wet' slab crust proximal to the edges of slab windows at depths of 25-90 km, whereas non-adakitic melts of granodiorite to tonalitic compositions are generated along plate edges at depths of 5-65 km. Such compositions are not recognized in the Antarctic Peninsula, even in trench proximal locations. The Antarctic Peninsula has a unique ridge-crest-trench collision history because all collisions were near-orthogonal to the continental margin. At most other locations along the Pacific margin of the America, ridge subduction was strongly oblique, or slab windows formed by ridge-crest–trench–

transform interactions (Thorkelson et al. 2011). In these cases, the oceanic crust forming the edge of the slab window was of variable age and potentially considerably older than any of the oceanic crust being subducted along the Antarctic Peninsula, was probably hydrated and capable of melting in water saturated conditions to produce adakite–tonalite magmatism (Thorkelson & Breitsphrecher 2004)

In the case of the Antarctic Peninsula, because subduction ceased following orthogonal ridge-crest–trench collisions, the oceanic crust beneath the continental margin was both young and hot at the time of collision and the trailing edge of the slab forming the eastern margin of the slab window was necessarily zero age at the instant of its subduction. Barker (1982) estimated that the age of the subducted oceanic lithosphere at 100km depth at the time of ridge-crest-trench collisions along the northern part of the Antarctic Peninsula as far north as the South Anvers fracture zone was a maximum of ~20 Ma but in the south of the Peninsula this was nearer 11 Ma. Consequently, the geometry of slab window formation controls the age and thus thermal state of the oceanic crust being subducted. The young age of the oceanic lithosphere being subducted along the Antarctic Peninsula suggests that it was unlikely to be hydrated at the time of ridge crest trench collision, and in any case, rapid prograde metamorphism to eclogite facies would have rendered the crust anhydrous soon after subduction. In eastern Papua New Guinea, it has been shown that the transformation of oceanic crust into anhydrous coestite-bearing eclogite under ultra-high–pressure conditions of up to 3.0 GPa and 800°C occurs over the same timescales a plate tectonics. Eclogites at D'Entrecasteaux Island, at the boundary of the Woodlark and Australian plates, are dated at 4.33 Ma meaning that the entire cycle of subduction, prograde metamorphism and exhumation took place over an exceedingly short timescale (Baldwin et al. 2004). Therefore, there is evidence to support the possibility and probability of transforming young, hot oceanic crust into eclogite over short timescales. Once transformed into garnet eclogite or pyroxenite the slab was able to contribute near-dry melts.

Remaining conundrums

Whereas melting of slab-hosted pyroxenite provides a very viable alternative to melting at elevated T_P or with CO_2 on the solidus, some aspects of the post-subduction magmatism remain unanswered. For example, the situation at James Ross Island remains rather enigmatic. Here, alkali basalt erupted, but this is essentially a back-arc rather than slab window setting. At the South Shetland Islands, subduction activity decreased sharply after 6 Ma and stopped or became very slow after the cessation of spreading in Drake Passage at about 3.3 Ma (Jin et al. 2009). The present extension in Bransfield Rift started less than 4 m.y. ago, and possibly less than 1.5 m.y. ago, following the demise of the Antarctic-Phoenix spreading centre at about ~3.5 Ma (Lawver

et al. 1995; Keller et al. 2002). One possibility is that once subduction slowed dramatically at the South Shetland Islands Trench, then a remnant subducted slab might be present as far east as the back-arc, and it is this that underwent melting to produce the James Ross Island Volcanic Group.

Miocene volcanism at the Jones Mountains (Hole et al. 1993b), 750km WSW of Alexander Island, share geochemical affinities with the Antarctic Peninsula occurrences, and do not appear to form part of the larger Marie Byrd Land province of West Antarctica. This being the case, any attempt to explain the Antarctic Peninsula volcanism in relationship to slab window formation, must also account for the origin of the Jones Mountains occurrences. However, Hole et al. (1993b) noted that the Jones Mountains sits astride the projected position of the Undinsev Fracture Zone, which was the locus of the earliest Ridge-crest-trench between a segment of the Antarctic-Phoenix spreading centre and the continental margin (Hole et al. 1993b).

A particularly critical issues is the age and timing of post-subduction volcanism in relationship to cessation of subduction. Reliable geochronological data are non-existent for many of the key exposures described here, and a concerted campaign of dating these fascinating, but somewhat enigmatic rocks, would further improve our understanding of the relationship between alkalic volcanism and slab-window formation.

Acknowledgements

Investigations into alkali basalts in the Antarctic Peninsula were made when MJH was an employee of the British Antarctic Survey. The number of people who made the fieldwork possible are too numerous to mention, but to anyone involved in the 1983-84, 85-86 and 87-88 Austral Summer field seasons, I owe a debt of gratitude. The manuscript was improved by the thoughtful reviews of Kurt Panter and John Gamble. The late Peter Barker first introduced me to the complexities of ridge-crest trench interactions and for that I will also be grateful.

Chapter 4. Post-subduction, alkaline volcanism – Petrology & Petrogenesis

References cited.

Baldwin, S.L., Monteleone, B.B., Webb, L.E. Fitzgerald, P.G., Grove, M. & Hill, E.J. 2004. Pliocene eclogite exhumation at plate tectonic rates in eastern Papua New Guinea. Nature, 431, 263-267. DOI: 10.1038/nature02846

Barker, P.F. 1982. The Cenozoic subduction history of the Pacific margin of the Antarctic Peninsula: ridge crest-trench interactions. Journal of the Geological Society, London, 139, 787-801.

Bevier, M.L. 1983. Implications of chemical and isotopic composition for petrogenesis of Chilcotin group basalts, British Columbia. Journal of Petrology, 24, 207-226.

Breitsprecher, K. & Thorkelson, D.J. 2009. Neogene kinematic history of Nazca-Antarctic-Phoenix slab windows beneath Patagonia and the Antarctic Peninsula. Tectonophysics, 464, 10-20.

Choe, W-H., Lee, J-I., Lee, M-J., Hur, S-D. & Jin, Y-K. 2007, Origin of E-MORB in a fossil spreading center: the Antarctic-Phoenix Ridge, Drake Passage, Antarctica. Geosciences, Journal, 11, 186-199. DOI: 10.1007/BF0291393

Choi, S-H, Schiano, P., Chen, Y., Devidal, J-L, Choo, M-K, & Lee, J-I. 2013, Melt inclusions in olivine and plagioclase phenocrysts from Antarctic–Phoenix Ridge basalts: Implications for origins of N- and E-type MORB parent magmas. Journal of Volcanology and Geothermal Research, 253, 75-86. DOI: 10.1016/j.jvolgeores.2012.12.008

Danyushevsky, L.V. & Plechov P. 2011, Petrolog3: Integrated software for modeling crystallization processes: Geochemistry Geophysics Geosystems, 12. DOI:10.1029/2011GC003516

Dasgupta, R., Hirschmann, M. M., & Smith N. D. 2007. Partial melting experiments on peridotite+CO_2 at 3 GPa and genesis of alkalic ocean island basalts. Journal of Petrology, 48, 2093– 2124.

Dasgupta, Mallik, A., Tsuno, K., Withers, A.C., Hirth, G. & Hirschmann, M.M. 2013. Carbon-dioxide-rich silicate melt in the Earth's upper mantle. Nature, 493, 211-216. doi:10.1038/nature11731

Dickinson, W. R. & Snyder, W. S. 1979. Geometry of subducted slabs related to the San Andreas transform. Journal of Geology, 87, 609-627.

D'Orazio, M.D., Agostini, S., Innocenti, F., Haller, M.J., Manetti, P. & Mazzarini, F. 2001 Slab window-related magmatism from southernmost South America: the Late Miocene mafic volcanics from the Estancia Glencross Area (~52°S, Argentina–Chile). Lithos, 57, 67-89

Eagles, G., Gohl, K. & Larter, R.D. 2007. High-resolution animated tectonic reconstruction of the South Pacific and West Antarctic Margin. Geochemistry, Geophysics, Geosystems, 5. DOI: 10.1029/2003GC000657

Grove, T. L., Till, C.B. & Krawczynski, M.J. 2012. The role of H_2O in subduction zone magmatism. Annual Reviews of Earth and Planetary Sciences, 40, 413-439. 10.1146/annurev-earth-042711-105310

Hacker, B.R., Peacock, S.M., Abers, G.A. & Holloway, S.D. 2003. Subduction Factory II: Are intermediate-depth earthquakes in subducting slabs linked to metamorphic dehydration reactions? Journal of Geophysical Research, 108. doi:10.1029/2001JB001129

Hart, S.R. 1988. Heterogeneous mantle domains: signatures, genesis and mixing chronologies. Earth and Planetary Science Letters 90, 273-96.

Herzberg, C., 2006. Petrology and thermal structure of the Hawaiian plume from Mauna Kea volcano. Nature, 444, 605-609. DOI:10.1038/nature05254

Herzberg, C., 2011. Identification of source lithology in the Hawaiian and Canary Islands: implications for origins. Journal of Petrology, 52, 113-146. DOI:10.1093/petrology/egq075

Herzberg, C., & Asimow P.D. 2008, Petrology of some oceanic island basalts: PRIMELT2.XLS software for primary magma calculation. Geochemistry Geophysics Geosystems, 9. DOI: 10.1029/2008GC002057

Herzberg C, & Asimow P.D. 2015, PRIMELT3 MEGA.XLSM software for primary magma calculation: Peridotite primary magma MgO contents from the liquidus to the solidus. Geochemistry Geophysics Geosystems. DOI: 16: 563-578. 10.1002/2014GC005631

Hirschmann, M.M. 2000. Mantle solidus: Experimental constraints and the effects of peridotite composition. Geochemistry, Geophysics, Geosystems, 1. DOI: 10.1029/2000GC000070

Hole, M.J. 1988. Post-subduction alkaline volcanism along the Antarctic Peninsula. Journal of the Geological Society, London, 145, 985-989.

Hole, M.J. 1990a. Geochemical evolution of Pliocene-Recent post-subduction alkalic basalts from Seal Nunataks, Antarctic Peninsula: Journal of Volcanology and Geothermal Research, 40**,** 149-167. DOI: 10.1016/0377-0273(90)90118-Y

Hole M.J. 1990b. Beethoven Peninsula. Antarctic Research Series, 48, 268-270.

Hole M.J. 1990c. Hornpipe Heights. Antarctic Research Series, 48, 270-272.

Hole, M.J. 2018. Mineralogical and geochemical evidence for polybaric fractional crystallization of continental flood basalts and implications for identification of peridotite and pyroxenite source lithologies. Earth Science Reviews, 176, 51-67. DOI: 10.1016/j.earscirev.2017.09.014

Chapter 4. Post-subduction, alkaline volcanism – Petrology & Petrogenesis

Hole, M. J. & Thomson J.W. 1990. Mount Pinafore-Debussy Heights. Antarctic Research Series, 48, 268-270.

Hole, M.J. & LeMasurier, W.E. 1994. Tectonic controls on the geochemical composition of Cenozoic, mafic alkaline volcanic rocks from West Antarctica. Contributions to Mineralogy and Petrology, 117, 187-202.

Hole, M.J. & Saunders, A.D., 1996. The generation of small melt-fractions in truncated melt columns: Constraints from magmas erupted above slab windows and implications for MORB genesis. Mineralogical Magazine, 60, 173-189.

Hole, M.J. & Larter, R.D. 1993. Trench-proximal volcanism following ridge crest-trench collision along the Antarctic Peninsula. Tectonics, 12, p. 897-910. DOI: 10.1029/93TC00669

Hole, M.J. & Millett J.M. 2016. Controls of mantle potential temperature and lithospheric thickness on magmatism in the North Atlantic Igneous Province: Journal of Petrology, 57, 417-436. DOI: 10.1093/petrology/egw014

Hole, M.J., Rogers, G., Saunders, A.D. & Storey, M. 1991, Relation between alkalic volcanism and slab-window formation. Geology, 19, p. 657-660. DOI: 10.1130/0091-7613(1991)

Hole, M.J., Kempton, P.D. & Millar, I.L. 1993, Trace-element and isotopic characteristics of small-degree melts of the asthenosphere: Evidence from the alkalic basalts of the Antarctic Peninsula. Chemical Geology, 109, p. 51-68. DOI: 10.1016/0009-2541(93)90061-M

Hole, M.J., Saunders, A.D., Rogers, G., & Sykes, M.A., 1994a. The relationship between alkaline magmatism, lithospheric extension and slab window formation along continental destructive plate margins. In: Smellie, J.L. (ed) Volcanism associated with extension at consuming plate margins. Geological Society, London, Special Publications, 81, 265-285. DOI: 10.1144/GSL.SP.1994.081.01.15

Hole, M.J., Storey, B.C. & LeMasurier, W.E. 1994b. Tectonic setting and geochemistry of Miocene alkalic basalts from the Jones Mountains, West Antarctica. Antarctic Science, 6, 85-92.

Homrighausen, S., Hoernle, K., Hauff, F., Geldmacher, J., Wartho, J-A, van den Bogaard, P. & Garbe-Schonberg, D. 2018. Global distribution of the HIMU end member: Formation through Archeanplume-lid tectonics. Earth Science Reviews, 182, 85-101.

Jin, Y.K., Lee, J., Hong, J.K. & Nam, S.H. 2009. Is subduction ongoing in the South Shetland Trench, Antarctic Peninsula? New constraints from crustal structures of outer trench wall Geoscience Journal, 13, 59-67. DOI 10.1007/s12303-009-0005-5

Johnson, S.T. & Thorkelson, D.J. 2000. Continental flood basalts: Epispodic magmatism above long-lived hotspots. Earth and Planetary Science Letters, 175, 247-256.

Chapter 4. Post-subduction, alkaline volcanism – Petrology & Petrogenesis

Johnston, A.D. & Draper, D.S. 1992. Near-liquidus phase relations of an anhydrous high-magnesia basalt from the Aleutian Islands: Implications for arc magma genesis and ascent. Journal of volcanology & Geothermal Research, 52, 27-41.

Keller, R.A., Fisk, M.R., Smellie, J.L. & Strelin, J.A. 2002. Geochemistry of back arc basin volcanism in Bransfield Strait, Antarctica: Subducted contributions and along-axis variations. Journal of Geophysical Research, 107, 2171. DOI 10.1029/2001JB000444/

Keshav, S., Gudfinnson, G.H. Sen, G. & Fei, Y. 2004. High-pressure melting experiments on garnet clinopyroxenite and the alkalic to tholeiitic transition in ocean-island basalts. Earth and Planetary Science Letters, 223, 356-379.

Kogiso, T, Hirschmann, M.M. & Frost, D.J. 2003. High-pressure partial melting of garnet pyroxenite: Possible mafic lithologies in the source of ocean island basalts. Earth and Planetary Science Letters, 216, 603-617.

Kosler, J., Magna, T., Mlcoch, B., Mixa, P. Nyvlt, D. & Holub, F.V. 2009. Combined Sr, Nd, Pb and Li isotope geochemistry of alkaline lavas from northern James Ross Island (Antarctic Peninsula) and implications for back-arc magma formation. Chemical Geology, 258, 207-218

Lambart, S. 2017. No direct contribution of recycled crust in Icelandic basalts. Geochemical Perspectives Letters, 4, 7-12.

Lambart, S, Laporte, D. & Schiano, P. 2009. An experimental study of pyroxenite partial melts at 1 and 1.5 GPa: Implications for the major-element composition of Mid-Ocean Ridge Basalts. Earth and Planetary Science Letters, 288. 335-347.

Lambart, S., Laporte, D., Provost, A. & Schiano, P. 2012. Fate of pyroxenite-derived melts in the peridotitic mantle: thermodynamic and experimental constraints. Journal of Petrology 53, 451-476.

Lambart, S., Laporte, D., Provos, A. & Schiano, P. 2013. Markers of the pyroxenite contribution in the major-element compositions of oceanic basalts: Review of the experimental constraints. Lithos, 160-161, 14-36.

Lambart. S., Baker, M.B. & Stopler, E.M. 2016. The role of pyroxenite in basalt genesis: Melt-PX, a melting parameterization for mantle pyroxenites between 0.9 and 5GPa. Journal of Geophysical Research, Solid Earth, 121, 5708-5735. doi: 10.1002/2015JB012762.

Larter, R.D. & Barker, P.F. 1991. Effects of ridge-crest trench interaction on Antarctic-Pheonix spreading: forces on a young subducting plate. Journal of Geophysical Research, 96 (B12) 19583-19607.

Chapter 4. Post-subduction, alkaline volcanism – Petrology & Petrogenesis

Lawver, L.A., Keller, R.A., Fisk, M.R. & Strelin, J.A. 1995. Bransfield Strait, Antarctic Peninsula Active Extension behind a Dead Arc. In: Taylor B. (eds) Backarc Basins. Springer, Boston, MA.

Le Bas. M.J. & Strekheisen, A.L. 1991. The IUGS systematics of igneous rocks. Journal of the Geological Society, London, 148, 825-833.

Martin, A.P., Cooper, A.F. & Price, R.C. 2013. Petrogenesis of Cenozoic, alkalic volcanic lineages at Mount Moring and their entrained lithospheric mantle xenoliths: lithospheric versus asthenospheric mantle sources. Geochimica et Cosmochimica Acta, 122, 127-152.

McKenzie, D.P. & O'Nions, R.K. 1995. The source region of Ocean Island basalts. Journal of Petrology, 36, 133-159.

O'Hara, M. J. 1968. The bearing of phase equilibria studies in synthetic and natural systems on the origin of basic and ultrabasic rocks. Earth Science Reviews 4, 69-133.

Palacz, Z. & Saunders, A.D. 1986. Coupled trace element and isotope enrichment in the Cook-Austral-Samoa Island, southwestern Pacific. Earth and Planetary Science Letters. 79, 270-280.

Pertermann, M. & Hirschmann, M.M. 2003. Partial melting experiments on a MORB-like pyroxenite between 2 and 3 GPa: Constraints on the presence of pyroxenite in basalt source regions from solidus location and melting rate. Journal of Geophysical Research, 108(B2), 2125.

Pertermann, M., Hirschmann M.M., Hametner, D., Günther, D. & Schmidt, M.W. 2004. Experimental determination of trace element partitioning between garnet and silica-rich liquid during anhydrous. Geochemistry Geophysics Geosystems, 5. doi:10.1029/2003GC000638

Putirka, K.D., 2008. Thermometers and barometers for volcanic systems. In: Putirka, K. D., and Tepley, F. J., III (eds) Minerals, Inclusions and Volcanic Processes. Mineralogical Society of America and Geochemical Society, Reviews in Mineralogy and Petrology, 69, 61–120. DOI: 10.2138/rmg.2008.69.3

Rhodes J. M. & Vollinger, M. J. 2004. Composition of basaltic lavas samples by phase-2 of the Hawaii Scientific Drilling Project: geochemical stratigraphy and magma types. Geochemistry, Geophysics, Geosystems 5. DOI: 10.1029/2002GC000434

Sarafian, E., Gaetini, G.A., Hauri, E.H. & Sarafian, A.R. 2017. Experimental constraints on the damp peridotite solidus and oceanic mantle potential temperature. Science, 355, 942-945. DOI: 10.1126/science.aaj2165

Chapter 4. Post-subduction, alkaline volcanism – Petrology & Petrogenesis

Saunders, A.D. 1982. Petrology and geochemistry of alkali-basalts from Jason Peninsula, Oscar II Coast, Graham Land. British Antarctic Survey Bulletin, 55, 1-9.

Smellie, J. L. 1987. Geochemistry and tectonic setting of alkaline volcanic rocks in the Antarctic Peninsula: a review. Journal of Volcanology and Geothermal Research 32, 269-285.

Smellie, J.L. 1999. Lithostratigraphy of Miocene-Recent, alkaline volcanic fields in the Antarctic Peninsula and eastern Ellsworth Land. Antarctic Science, 11, 362-378.

Smellie, J.L., Pankhurst, R.J., Hole, M.J. & Thomson, J.W. 1988. Age, distribution and eruptive conditions of late Cenozoic alkaline volcanism in the Antarctic Peninsula and eastern Ellsworth Land. British Antarctic Survey Bulletin, 80, 21-49.

Sobolev, A.V., Hofmann, A.W., Sobolev, S.V., & Nikogosian, I.K. 2005. An olivine-free mantle source of Hawaiian shield basalts: Nature, 434, 590-597. doi: 10.1038/nature03411

Storey, M., Rogers, G., Saunders, A. D., & Terrell, D. 1989. San Quintin volcanic field, Baja California, Mexico: 'within-plate' magmatism following ridge subduction. Terra Nova 1, 195-202.

Sykes, M.A. 1988. The petrology and tectonic significance of the James Ross Island Volcanic Group, Antarctica. Unpublished PhD thesis, University of Nottingham. 218pp.

Sun, S- S. & McDonough, W. F. 1989. Chemical and isotopic systematics of oceanic basalts: implications for mantle composition and processes. In; A.D. Saunders & M. J. Norry (eds), Magmatism in the ocean basins. Geological Society Special Publication, 42, 313-345.

Thompson, R.N. 1982. Magmatism of the British Tertiary Volcanic Province (The Carnegie Review Article). Scottish journal of Geology, 18, 49-107.

Thorkelson, D.J. 1996. Subduction of diverging plates and the principles of slab window formation. Tectonophysics, 255, 47-63.

Thorkelson, D.J. & Taylor R.P. 1989. Cordilleran slab windows. Geology, 17, 833-836

Thorkelson, D.J. & Breitsprecher, K. 2004. Partial melting of slab window margins: Genesis of adakitic and non-adakitic magmas. Lithos, 79. 24-41.

Thorkelson, D.J., Madsen, J.K., & Sluggett, C.L. 2011, Mantle flow through the Northern Cordilleran slab window revealed by volcanic geochemistry: Geology, 39, 267-270. DOI: 10.1130/G31522.1;

Worner, G. Viereck, L.G., Hertogen, J. & Niephaus, H. 1989. The Mt Melbourne Volcanic Field (Victoria Land Antarctica) II. Geochemiistry and magma genesis. Geologische Jahrbuch, E38, 395-433.

Chapter 4. Post-subduction, alkaline volcanism – Petrology & Petrogenesis

Figure Captions.

Figure 1. Map of the Antarctic Peninsula showing the locations of the late Neogene volcanic fields (modified after Smellie, 1999).

Figure 2. Sketch maps of the Antarctic Peninsula and southern South America illustrating the tectonic setting and location of Antarctic-Phoenix Ridge at a) 15Ma and b) present-day. Triangle ornament represents active subduction and double lines represent spreading ridge segment. Abbreviations; NAI, Northern Alexander Island; SN, Seal Nunataks; JRI, James ross Island; BS, Bransfield Strait. After Hole & Larter (1993).

Figure 3. Cartoon illustrating the development of the slab window along the Antarctic Peninsula at present-day. Collision times for each ridge segment are given on the ocean-ward margin of the peninsula. After Hole *et al.* (1994a)

Figure 4. Plan view of slab window growth with time, showing the geographical location of the slab window-related basalts (open symbols with K-Ar age adjacent). The x-axis represents the palaeo-trench and the different ornaments correspond to the amount of slab window formation associated with each spreading ridge, the solid lines separating the ornaments being 'isochrons' for the slab window as a whole. The assumptions that are used in the calculations are that the angle of slab dip was ~45° and the rate of opening of an individual slab window segment was dependent on the spreading rate of the adjacent ridge crest to the north (see Barker 1982 and Larter & Barker 1991). It is also assumed that the subducted slab was planar, and the slab dip did not vary over time. Reducing the slab dip to 30 increases the linear width scale from 0 to 1400 km to 0 to 1650 km. After Hole *et al.* (1994a)

Figure 5. Total alkalis silica diagram (Le Bas & Streckheisen 1991) used for naming the volcanic rocks. Data sources; Saunders 1982; Hole 1988, 1990; Hole et al. 1993, 1994a, b; Sykes 1988; Smellie 1987; Smellie et al 1988; Kosler et al 2009; D'Orazio et al 2001.

Figure 6. CIPW normative tetrahedron projected from or to plagioclase onto the planes Ne-Ol-Di, Ol-Di-Hy and Hy-Di-Qz (Thompson 1982). Inverted triangles are CIPW norms for experimentally produced melts of pyroxenites 77SL-582 and MixG at 2.0 (grey) and 2.5 GPa (white) with the vector for increasing melting and increasing temperature shown (Keshav et al. 2004). Data for slab-window–related lavas from Estancia Glencross (white triangles) are from D'Orazio *et al.* (2001). Liquid lines of descent (LLD) along the cotectics L+Ol+Pl and L+Ol Pl+Cpx are taken from Hole (2018).

Figure 7. a) SiO_2; b) TiO_2; c) Al_2O_3 and d) CaO *versus* MgO for Antarctic Peninsula and Estancia Glencross post-subduction lavas. In c) and d) LLD were calculated from the most MgO-rich lava from Seal Nunataks (R.3735.1; 10.27 wt% MgO) using Petrolog3 and assuming

crystallization at the FMQ buffer (Danyuchevsky & Plechov 2011; Hole 2018). Sample R.3637.7 has a higher MgO content than R.3735.1, but the former has a significantly higher mode of olivine than the latter, but this is most likely a result of olivine accumulation. The field for East Pacific Rise MORB in a) and d) refer to N-MORB from the Siquieros Fracture Zone with data taken from PetDB. http://www.earthchem.org/petdb/

Figure 8. Primitive mantle (Sun & McDonough 1989) normalized incompatible trace element diagrams for a) Antarctic-Phoenix Ridge N- and E-MORB and trench proximal Dredge 138 lavas; b) basanite and tephrite from Northern Alexander Island; c) alkali olivine basalts and olivine tholeiites from Seal Nunataks and d) alkali basalts from James Ross Island. Data sources; a) Choi et al. 2013; Choe et al. 2007; Hole & Larter 1993; b) Hole 1988; c) Hole 1990; d) Kosler et al. 2009. The cross-hatched shading in b) to d) is the range for the Seal Nunataks lavas shown in c).

Figure 9. a) $^{207}Pb/^{204}Pb$ and b) $^{143}Nd/^{144}Nd$ *versus* $^{206}Pb/^{204}Pb$ and c) $^{143}Nd/^{144}Nd$ *versus* $^{87}Sr/^{86}Sr$ for the post subduction lavas. Data for Antarctic Phoenix N- and E-MORB are shown for comparison. Grey dots are the range of isotopic compositions for present day East Pacific Rise MORB (Data from PetDB https://www.earthchem.org/petdb – accessed May 2018). Data sources as for Fig. 8 except Seal Nunataks Hole et al. (1993). The northern Hemisphere Reference Line (NHRL) in b) is taken from Hart (1988).

Figure. 10 a) Pressure–temperature diagram showing the dry peridotite solidus (green curve) of Hirschmann (2000) and 'damp' solidus (blue pecked curve) with 450ppm H_2O (Sarafian et al. 2017) and generalized CO_2 saturated solidus (grey curve; Dasgupta et al. 2007). Isopleths for 5 –25% CO_2 in dry peridotite were calculated using the polynomial equations of Dasgupta (2013). The pecked portions of the curves are extrapolated from applied to the dry peridotite solidus of Hirschmann (2000). Garnet-in contour is taken from McKenzie & O'Nions (1995). The pecked portions of the curves are extrapolated from melting experiments at 2 GPa. Star in the circle is the PRIMELT3 solution for Antarctic-Phoenix Ridge N-MORB and the grey pecked line the adiabat for dry peridotite at T_P=1350°C (Herzberg & Asimow 2015; Hole & Millett 2016); b) CaO wt% *versus* SiO_2 wt% for Antarctic Peninsula post-subduction lavas and lavas from various volcanoes in the Ross Sea area of the West Antarctic Rift System which are denoted by crosses (Worner et al. 1989; Martin et al. 2013). The regions for melting of dry peridotite (green) and the dividing line between the compositions of melts from dry and carbonated peridotite are taken from Herzberg & Asimow (2008). The red squares represent the primary magma compositions

Chapter 4. Post-subduction, alkaline volcanism – Petrology & Petrogenesis

derived from melting of peridotite + CO_2 with wt% CO_2 on the solidus indicated. The red squares relate to the red solidi in a).

Figure 11. a) Pressure–temperature diagram illustrating the differences in melting behaviour for mantle peridotite and pyroxenites ID-16 (SE pyroxenite; Johnston & Draper 1992; Lambart et al. 2016) and M7-16 (SD pyroxenite; Lambart et al. 2009; 2012; 2016), mantle peridotite (Hirschmann 2000) and 'damp' peridotite (Sarafian et al. 2017). Garnet-in for peridotite is from McKenzie & O'Nions (1995) and for pyroxenite from Kogiso et al (2003). b) extent of melting (F wt%) *versus* pressure for peridotite M7-16. ID-16 has an almost identical melt productivity to M7-16. N-MORB is the final pressure of melting at the Antarctic-Phoenix Ridge based on PRIMELT3 solutions for melt inclusions in Choi et al. (2013).

Figure 12. a) CaO *versus* MgO for Seal Nunataks lavas (black dots) melt inclusions in Antarctic-Phoenix Ridge MORB (grey diamonds) and pyroxenite-derived lavas from Hawaii (grey dots; HSDP2). Grey squares represent parental, near-primary magmas to Seal Nuntaks lavas calculated by olivine addition and the use of the projections in Fig. 13. The star in the circle and black star are primary pyroxenite–derived magmas from Koolau and its Makapuu Stage respectively (Herzberg 2006; Sobolev et al. 2005) with the LLD for L+Ol for Makapuu shown (short pecks line). The pyroxenite-peridotite divide and the curved pecked lines representing the limits for primary magmas derived from mantle peridotite are both from Herzberg & Asimow (2008). b) SiO_2 *versus* MgO for Antarctic Peninsula post-subduction lavas, HSDP2 (grey dots with no border) and Koolau (crosses, KSDP; Koolau Scientific Drilling Project). The low and high SiO_2 trends are from Herzberg (2006).

Figure 13. a) Molecular projection from or towards olivine onto the plane CS–MS–A for Seal Nunataks parental pyroxenite-derived magmas (black dots). This projection is a larger portion of the garnet-pyroxene plane shown in b), and because the projection is from or towards olivine, olivine fractionation has no effect on the position of individual data points. The black curve separates olivine (to the left) and quartz (to the right) pyroxenite and the pecked curve represents the thermal divide at magma generation pressures, such that magmas to the right and left of the divide have divergent fractionation histories. In this projection Seal Nunataks lavas which have crystallized only olivine are related to cotectics at ~2.5-3.0 GPa. b) Molecular projection from or toward diopside onto the plane olivine–calcium Tschermak's molecule–quartz for Seal Nunataks parental pyroxenite-derived magmas (black dots). Parental compositions were calculated by adding equilibrium olivine to lavas that are related to the olivine liquidus until they reach the cotectic for the pressure

indicated by their position in the projection in a), that is between 2.5 and 3.0 GPa. The vertical pecked line is the garnet-pyroxene plane and separates silica-depleted and silica-enriched pyroxenite. Fields for basaltic oceanic crust (which give rise to silica enriched pyroxenite) and cumulates (which give rise to silica depleted pyroxenite) are taken from East Pacific Rise MORB glasses and their associated gabbroic cumulates (PetDB database and Herzberg 2011). Projection codes in mole% are from O'Hara (1968):

CS (Di) = $CaO+2(Na_2O+K_2O)–3{\cdot}333P_2O_5$

MS (Gt) = $2SiO_2+TiO_2–(FeO+MnO+MgO)–2CaO–8(Na_2O+K_2O)+6{\cdot}666P_2O_5$

A (En) = $TiO_2+Al_2O_3+Na_2O+K_2O$.

Ol = $0{\cdot}5(Al_2O_3+FeO+MnO+MgO)–0{\cdot}5(CaO+Na_2O+K_2O)+1.75P_2O_5$.

CaTs = $TiO_2+Al_2O_3+Na_2O+K_2O$

Qz = $SiO_2+TiO_2(0.5Al_2O_3)–0{\cdot}5(FeO+MnO+MgO)–1{\cdot}5CaO –$
$4.5(Na_2O+K_2O)+5.25P_2O_5$

Figure 14. Model melt compositions based on the trace element content of a typical example of oceanic crust (sample G2; Lambart 2017). The pressure for each model melt and the % melt production is given on the diagram. Model melts represent accumulated melt fractions calculated in increments of 1% melt over the range 5-25% melt using the method described in Lambart (2017). Bulk distribution coefficients for trace elements and the mineralogical composition of pyroxenite were taken from and Pertermann & Hirschmann (2003) and Pertermann et al. (2004). See text for discussion. Mauna Loa olivine tholeiite is taken from Rhodes & Vollinger (2004).

Figure 15. Cartoon cross-section illustrating the thermal structure of the northern Antarctic Peninsula subduction zone in a) at the instant of ridge-crest−trench collision and in b), after ridge-crest−trench collision and slab window formation. In a) note that the oceanic crust thins towards the trench as would be expected for the subduction of a young slab. The temperature contours (red lines) are modified after the 'hot' slab model of Hacker et al. (2003) and extents of melting to generate calc-alkaline subduction related magmas are taken from Grove et al. (2012). A 1350°C adiabat at the collided Antarctic-Phoenix ridge segment is assumed and the temperature-depth profile is indicated in blue lettering and lines. At this T_P, and for the dry solidus of Hirschmann et al. (2000) peridotite melting would commence at ~2.2 GPa (solid blue line). The pyroxenite solidus is shown for M7-16 and was calculated using Melt-PX (Lambart et al. 2016). For Tp=1350°C pyroxenite melting would commence at ~1390°C and ~3.5 GPa (solid green line). In b), grey lines are

the temperature contours from a), and red lines are estimated temperature contours after slab window formation. Note that the 1390°C temperature contour is shallower than the depth required to initiate melting of pyroxenite M7-16 a requirement of this model. Because the oceanic lithosphere is continuing to be subducted, melting can only occur over a very small temperature interval and therefore small melt fractions are produced.

Fig. 1

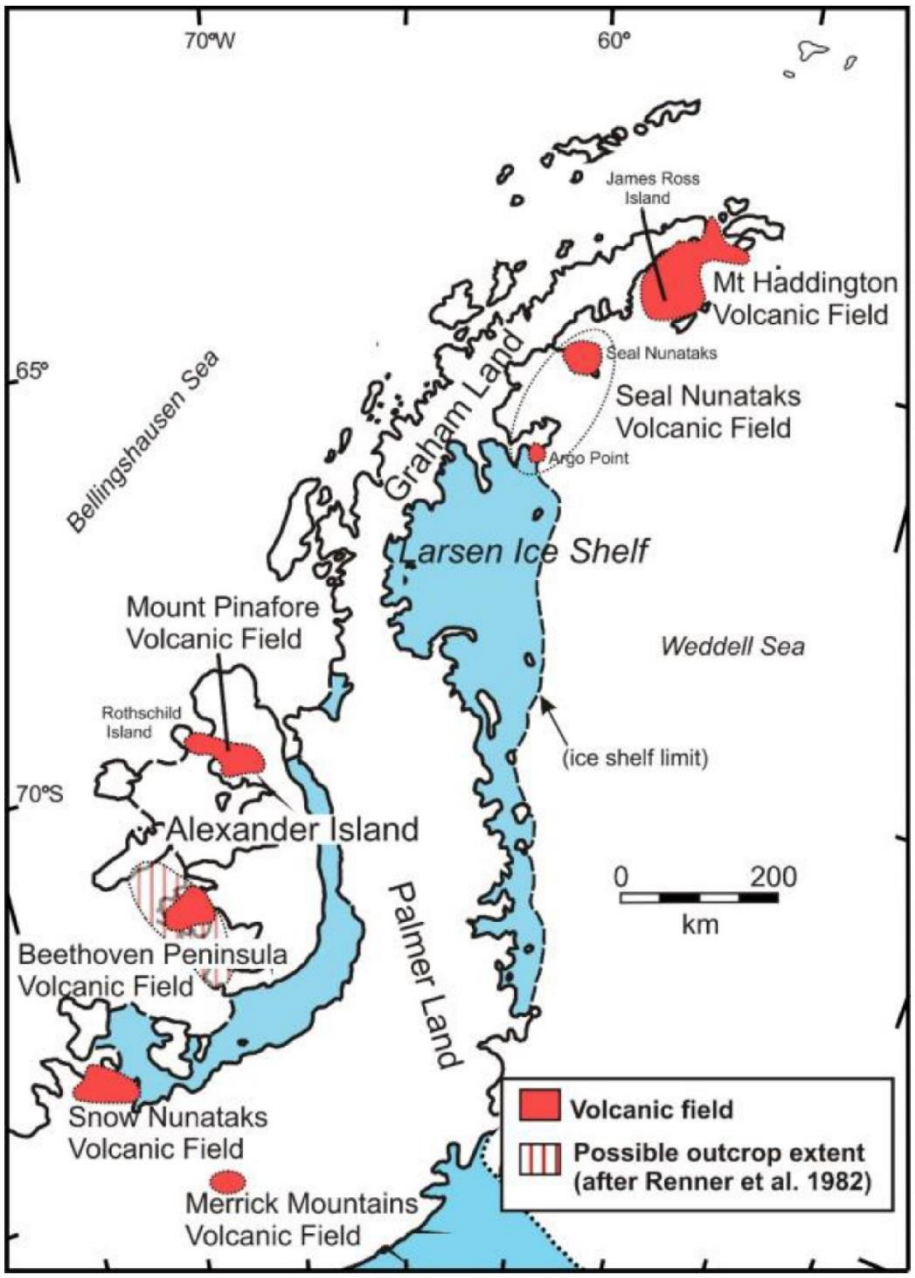

Chapter 4. Post-subduction, alkaline volcanism – Petrology & Petrogenesis

Fig. 2

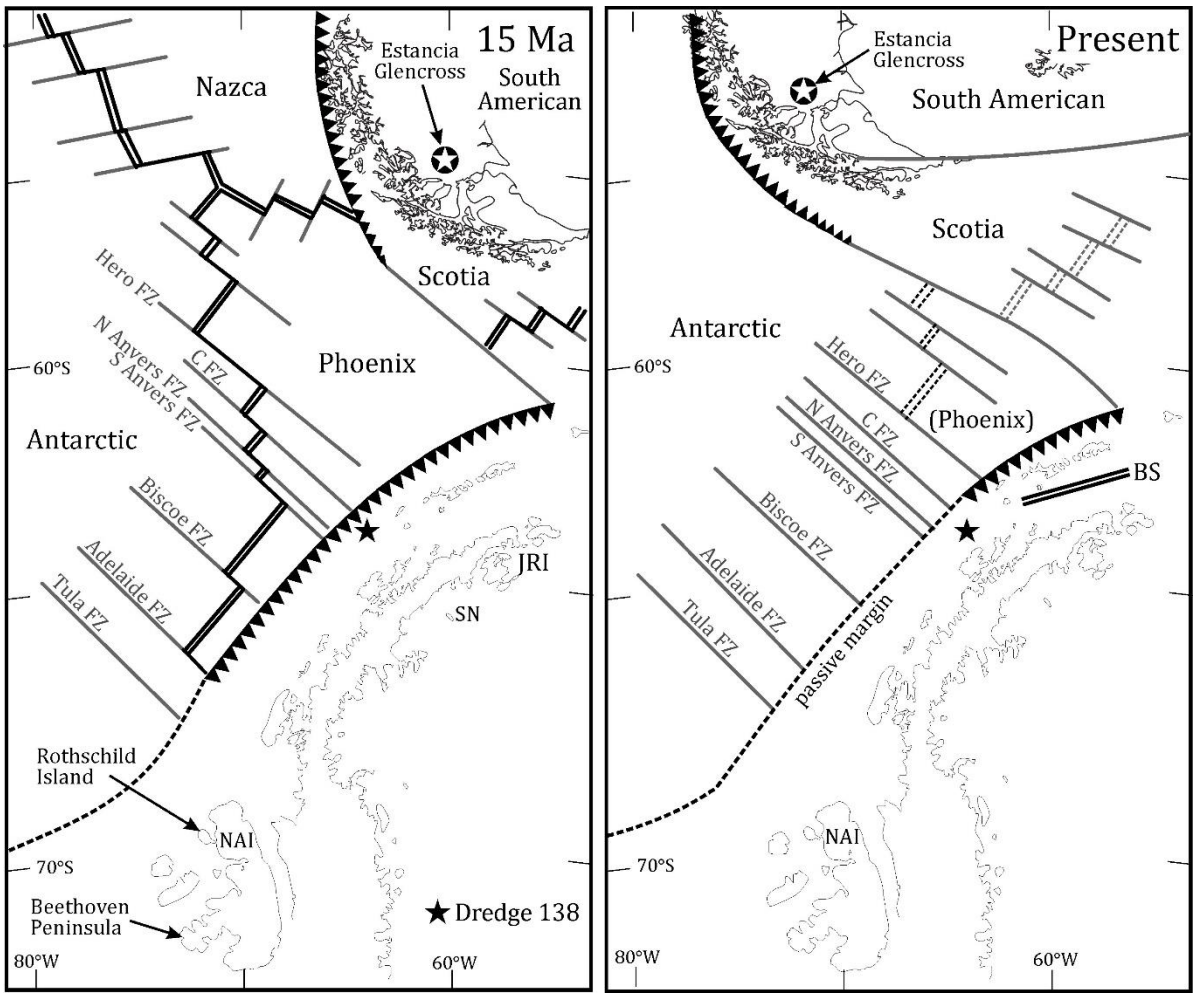
15 Ma
Nazca
Estancia
Glencross
South
American
Scotia
Hero FZ
N Anvers FZ
S Anvers FZ
C FZ
Phoenix
60°S
Antarctic
Biscoe FZ
Adelaide FZ
Tula FZ
JRI
SN
Rothschild
Island
NAI
70°S
Beethoven
Peninsula
Dredge 138
80°W
60°W
Present
Estancia
Glencross
South American
Scotia
Antarctic
60°S
Hero FZ
C FZ
N Anvers FZ
S Anvers FZ
(Phoenix)
BS
Biscoe FZ
Adelaide FZ
Tula FZ
passive margin
NAI
70°S
80°W
60°W

Fig. 3

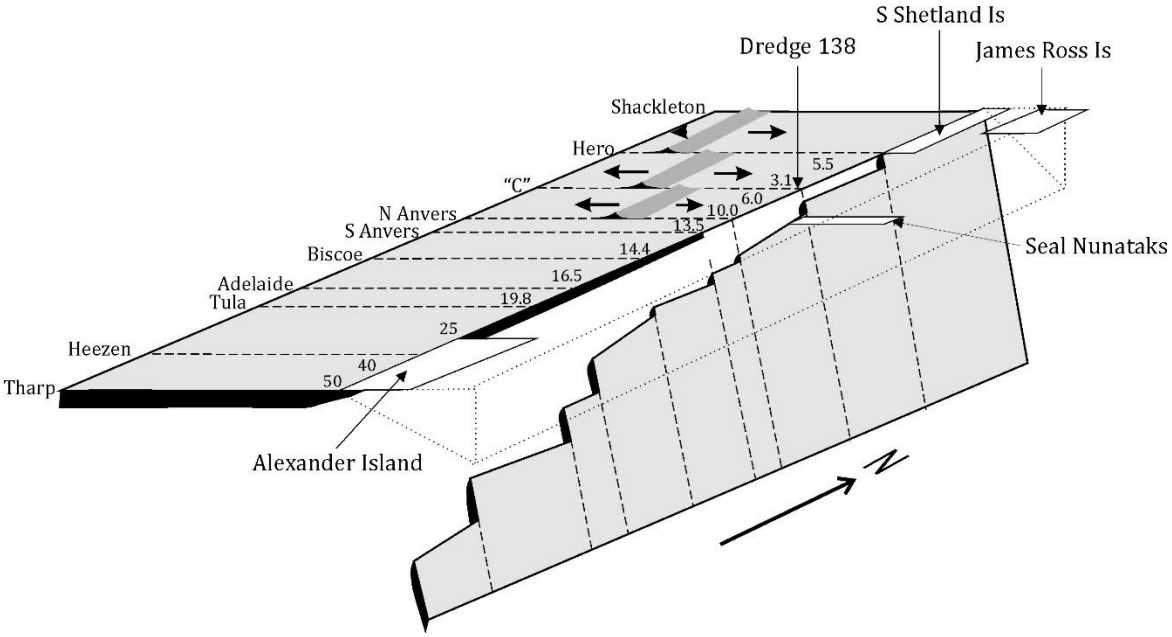
S Shetland Is
Dredge 138
James Ross Is
Shackleton
Hero
"C"
N Anvers
S Anvers
Biscoe
Adelaide
Tula
Heezen
Tharp
5.5
3.1
6.0
10.0
13.5
14.4
16.5
19.8
25
40
50
Seal Nunataks
Alexander Island
N

Fig. 4

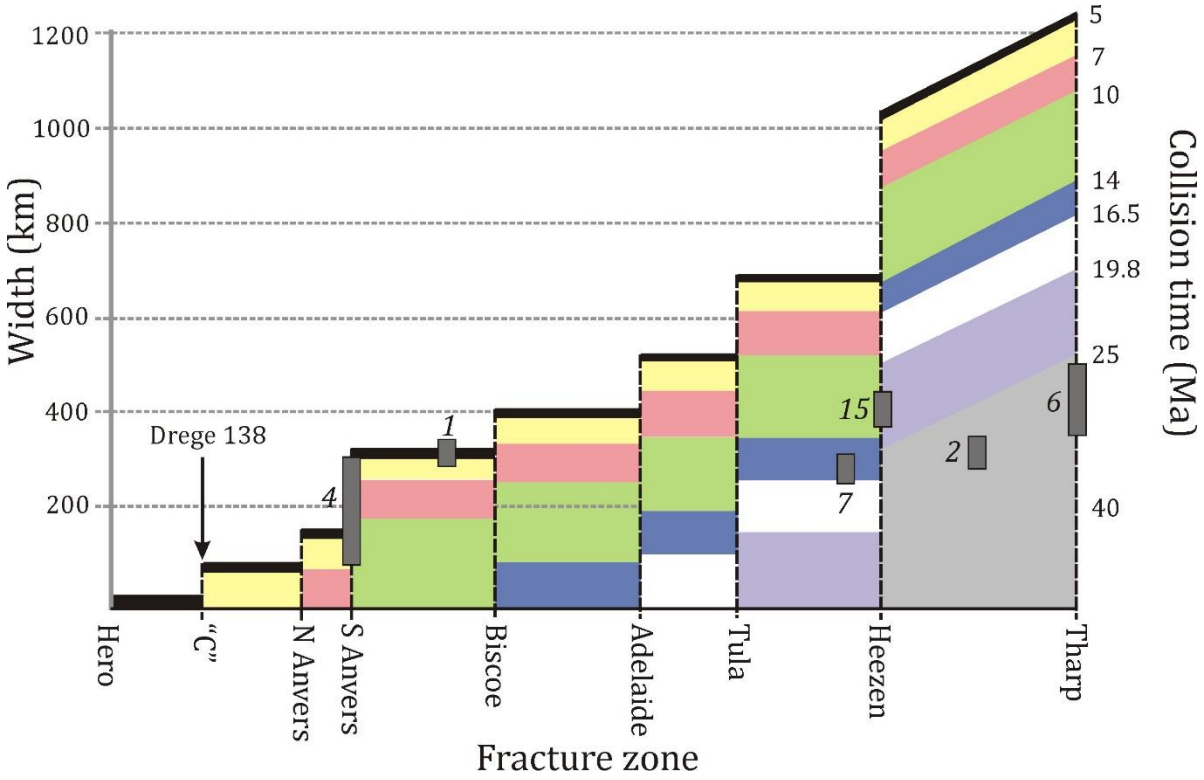
1200
1000
800
600
400
200
Width (km)
Drege 138
1
4
15
2
7
6
5
7
10
14
16.5
19.8
25
40
Collision time (Ma)
Hero
"C"
N Anvers
S Anvers
Biscoe
Adelaide
Tula
Heezen
Tharp
Fracture zone

Fig. 5

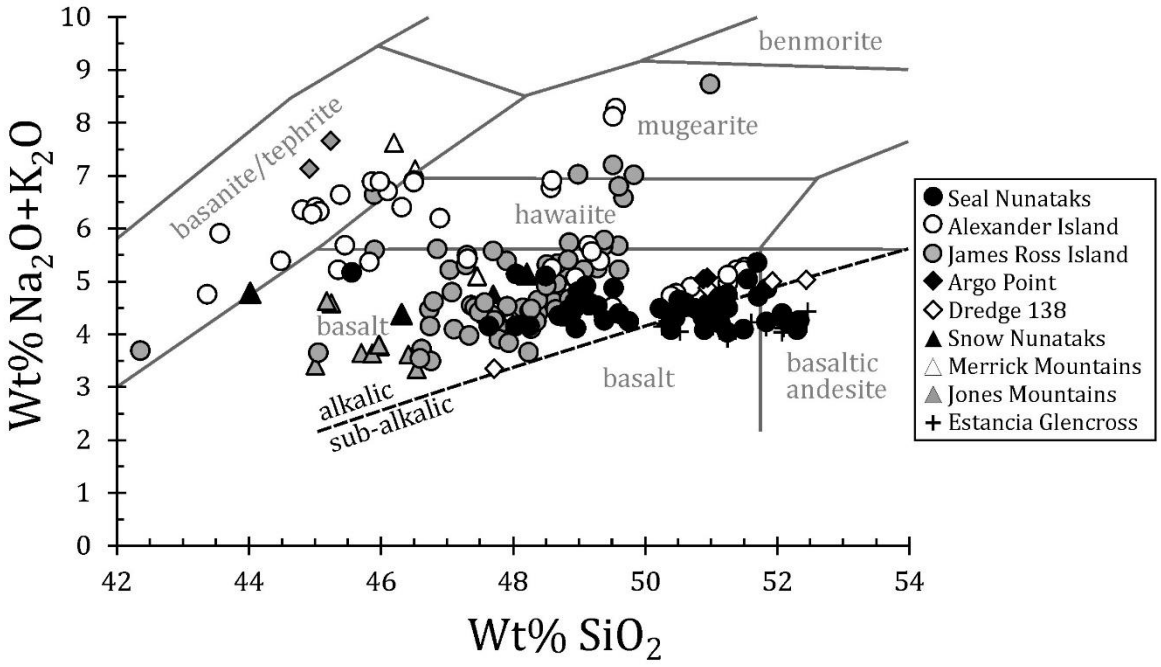
benmorite
mugearite
basanite/tephrite
hawaiite
basalt
basalt
basaltic andesite
alkalic
sub-alkalic
Seal Nunataks
Alexander Island
James Ross Island
Argo Point
Dredge 138
Snow Nunataks
Merrick Mountains
Jones Mountains
Estancia Glencross
Wt% Na2O+K2O
Wt% SiO2
0
1
2
3
4
5
6
7
8
9
10
42
44
46
48
50
52
54

Fig. 6

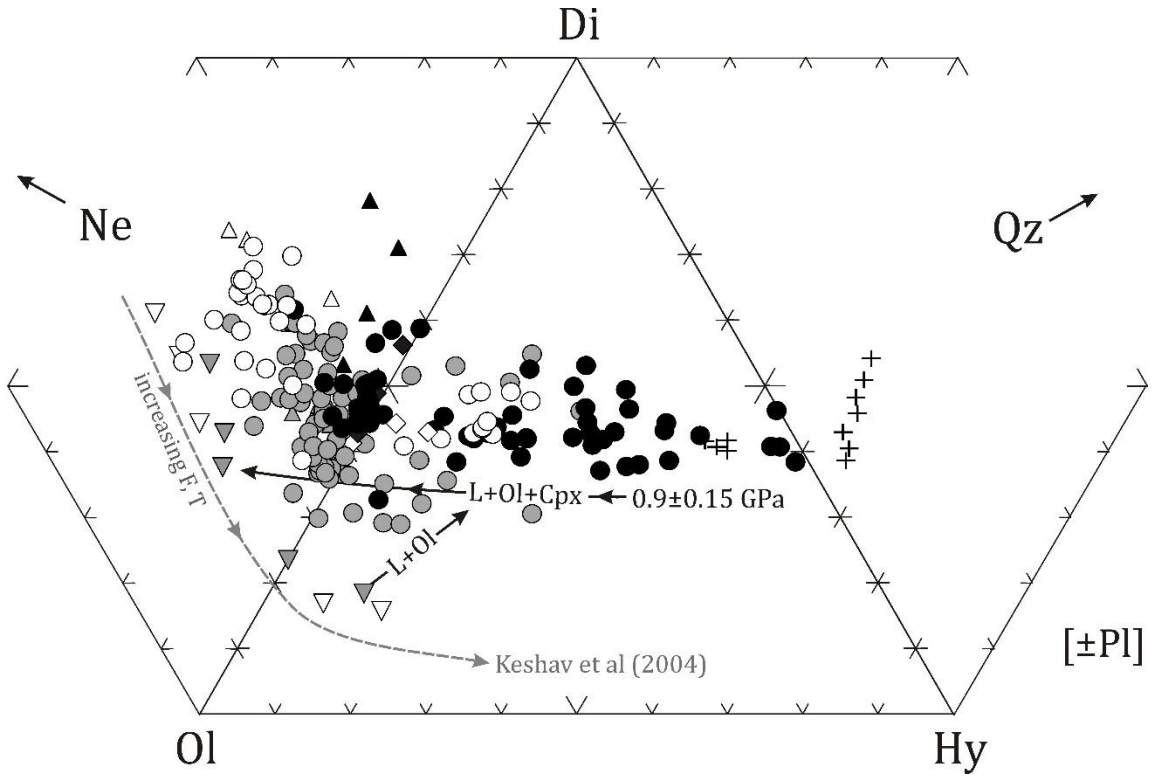
Di
Ne
Qz
[±Pl]
Ol
Hy
increasing F, T
L+Ol+Cpx
0.9±0.15 GPa
L+Ol
Keshav et al (2004)

Fig. 7

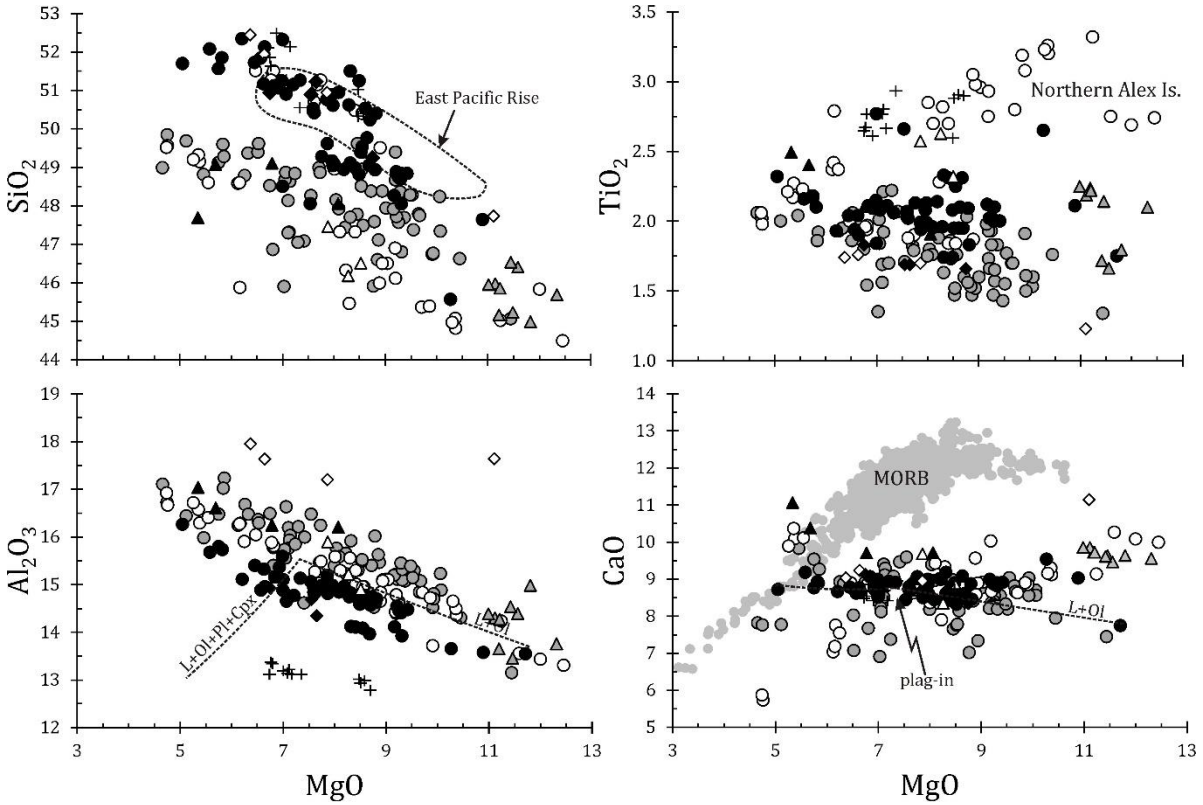
East Pacific Rise
Northern Alex Is.
MORB
L+Ol+Pl+Cpx
L+Ol
plag-in
SiO2
TiO2
Al2O3
CaO
MgO
MgO

Fig. 8

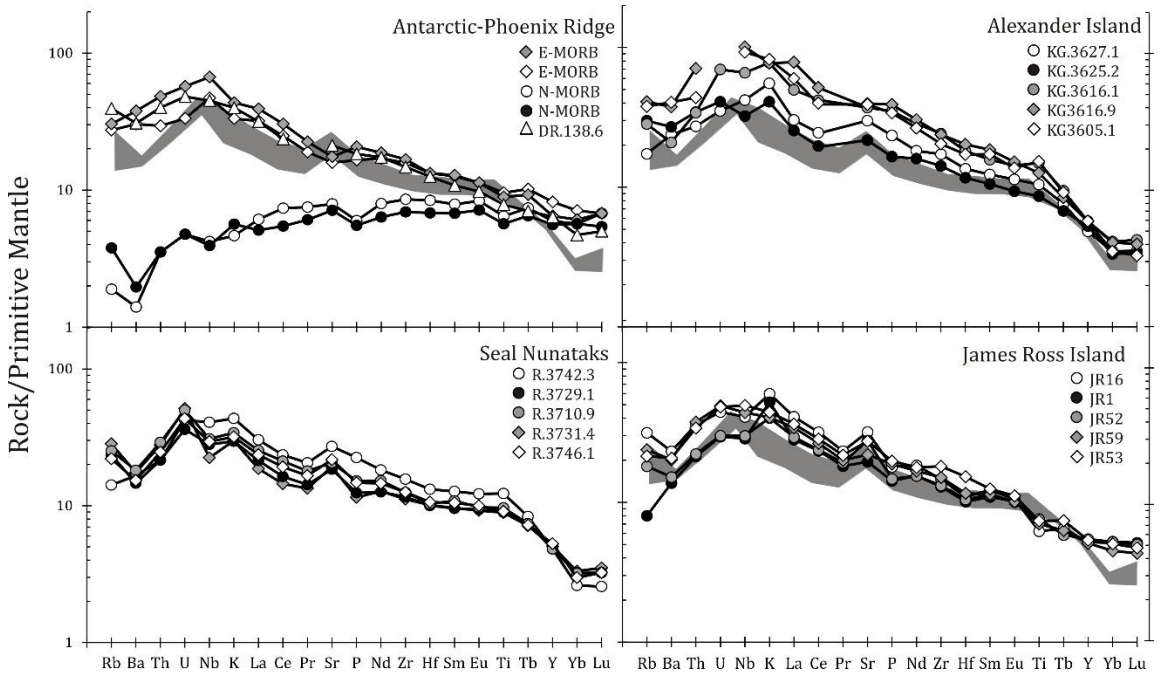
Antarctic-Phoenix Ridge
E-MORB
E-MORB
N-MORB
N-MORB
DR.138.6
Alexander Island
KG.3627.1
KG.3625.2
KG.3616.1
KG3616.9
KG3605.1
Seal Nunataks
R.3742.3
R.3729.1
R.3710.9
R.3731.4
R.3746.1
James Ross Island
JR16
JR1
JR52
JR59
JR53
Rock/Primitive Mantle
100
10
1
Rb Ba Th U Nb K La Ce Pr Sr P Nd Zr Hf Sm Eu Ti Tb Y Yb Lu

Fig. 9

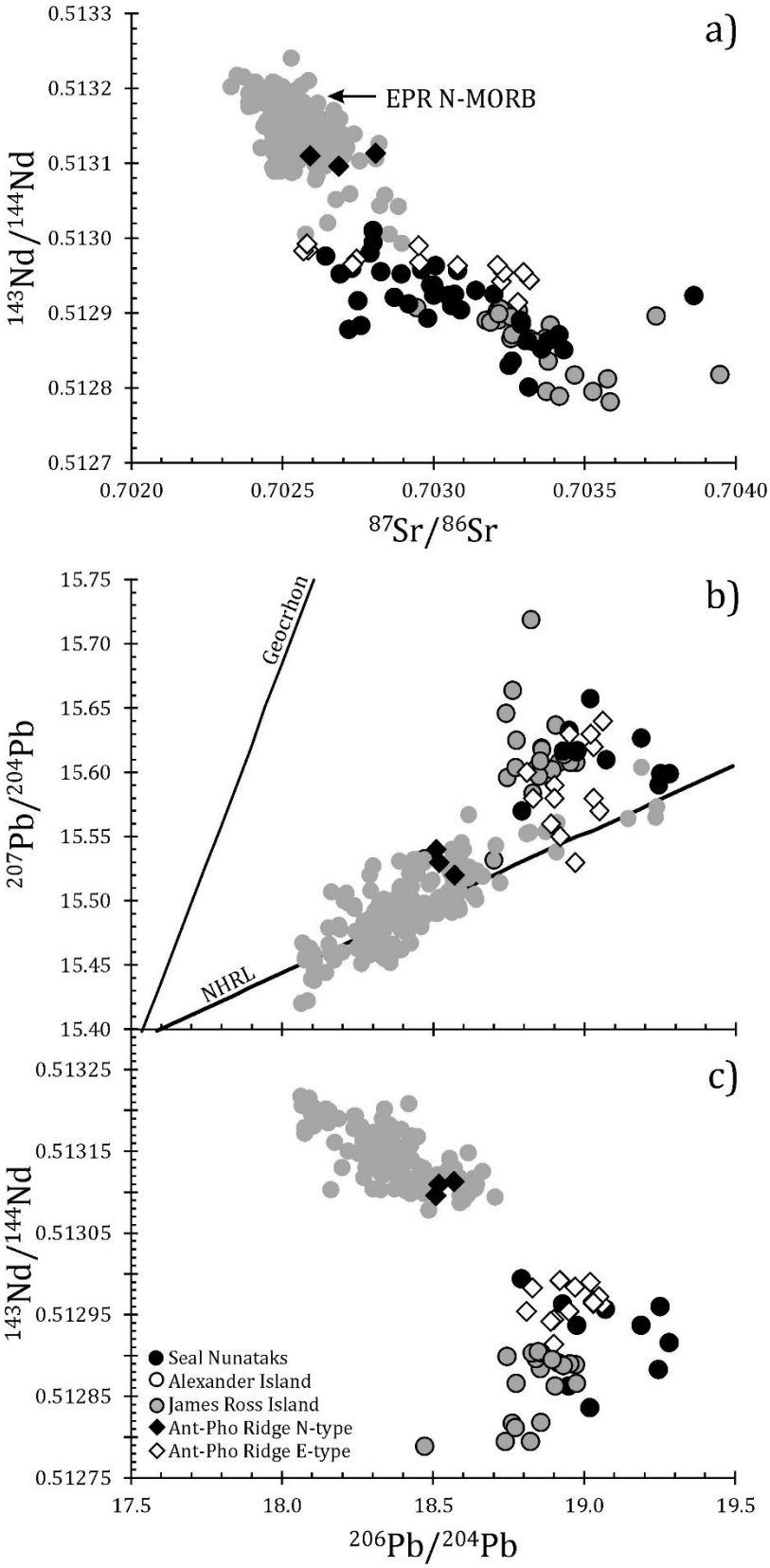
a)
EPR N-MORB
$^{143}Nd/^{144}Nd$
$^{87}Sr/^{86}Sr$
b)
Geochron
NHRL
$^{207}Pb/^{204}Pb$
c)
$^{143}Nd/^{144}Nd$
$^{206}Pb/^{204}Pb$
Seal Nunataks
Alexander Island
James Ross Island
Ant-Pho Ridge N-type
Ant-Pho Ridge E-type

Fig. 10

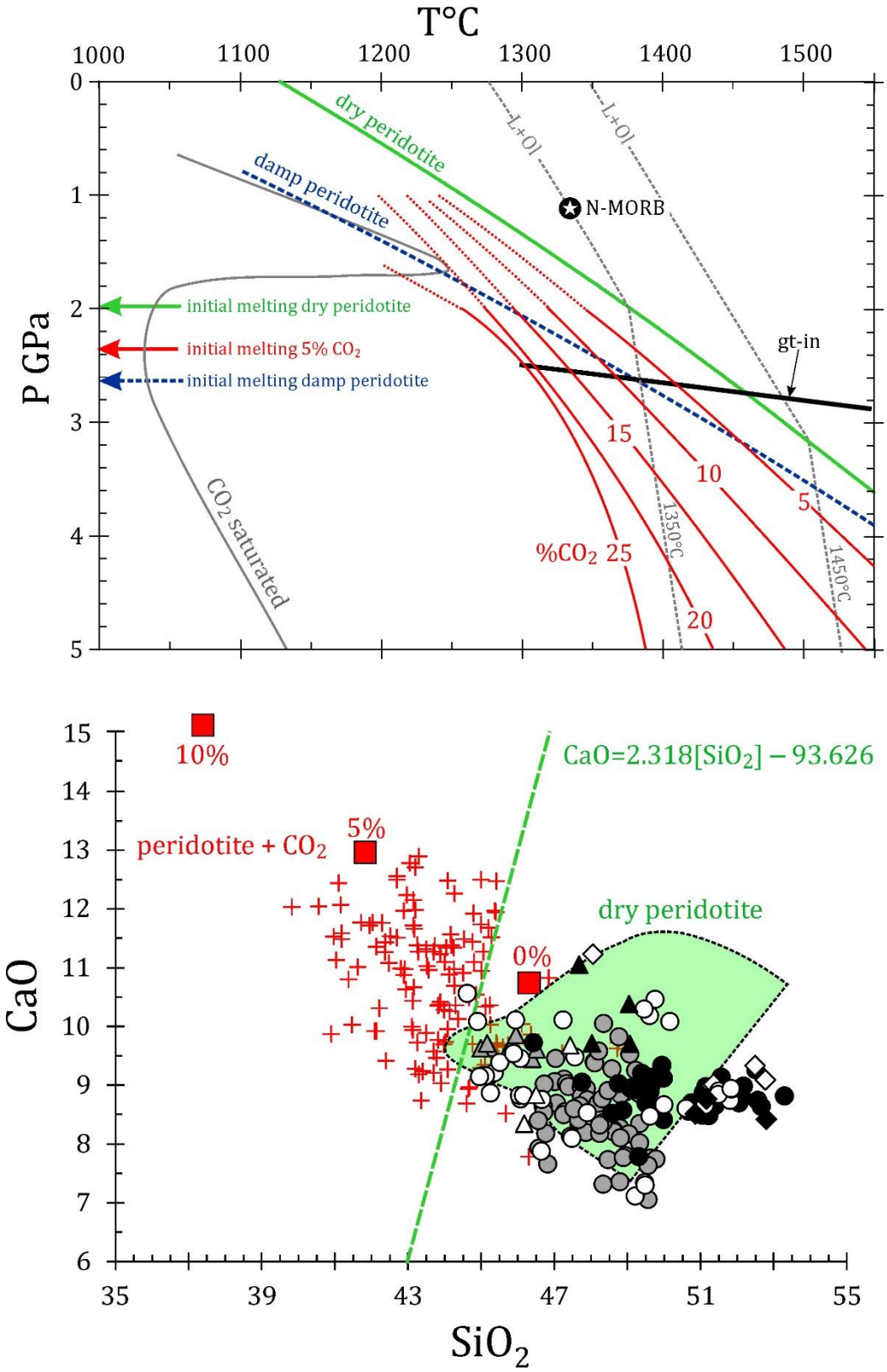
T°C
1000
1100
1200
1300
1400
1500
P GPa
0
1
2
3
4
5
dry peridotite
damp peridotite
L+Ol
L+Ol
N-MORB
initial melting dry peridotite
initial melting 5% CO2
initial melting damp peridotite
gt-in
15
10
5
%CO2 25
20
1350°C
1450°C
CO2 saturated
10%
5%
peridotite + CO2
0%
dry peridotite
CaO=2.318[SiO2] – 93.626
CaO
SiO2
15
14
13
12
11
10
9
8
7
6
35
39
43
47
51
55

Fig. 11

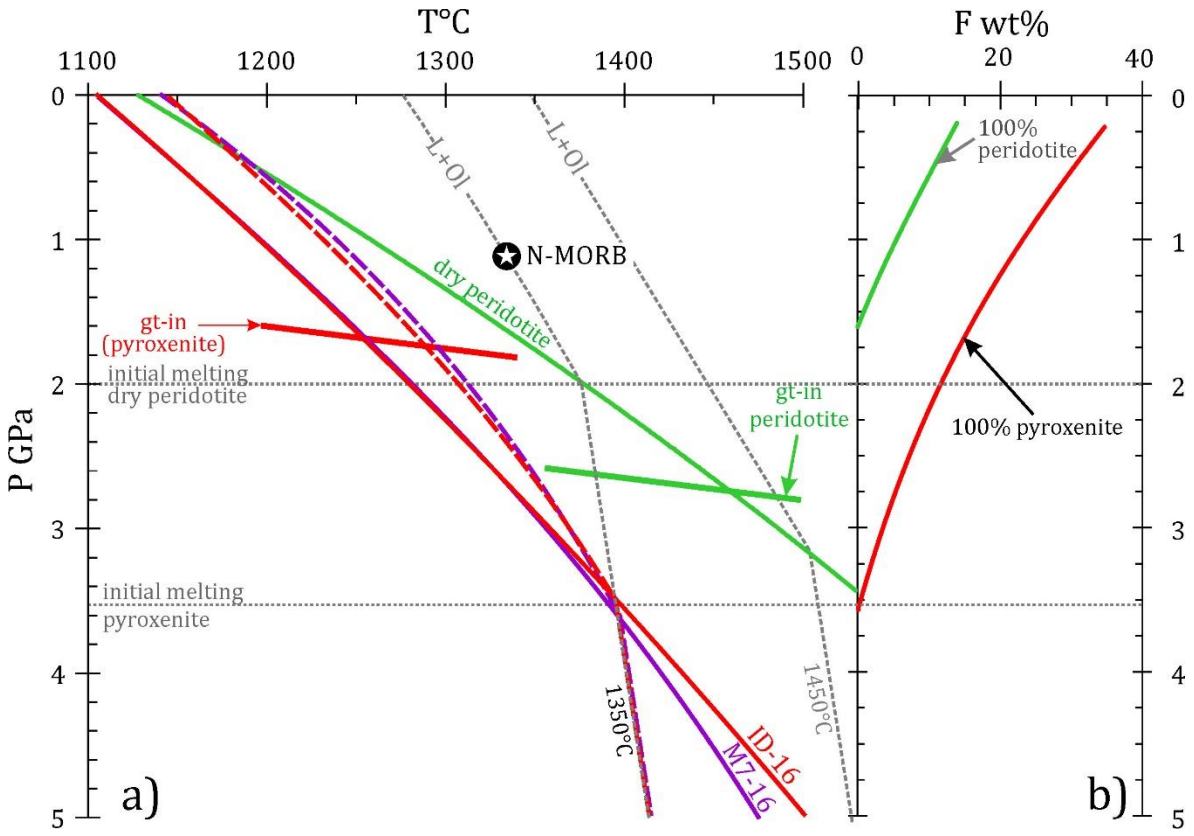
T°C
1100
1200
1300
1400
1500
F wt%
0
20
40
P GPa
0
1
2
3
4
5
L+Ol
L+Ol
N-MORB
dry peridotite
gt-in
(pyroxenite)
initial melting
dry peridotite
initial melting
pyroxenite
gt-in
peridotite
100%
peridotite
100% pyroxenite
1350°C
1450°C
ID-16
M7-16
a)
b)

Fig. 12

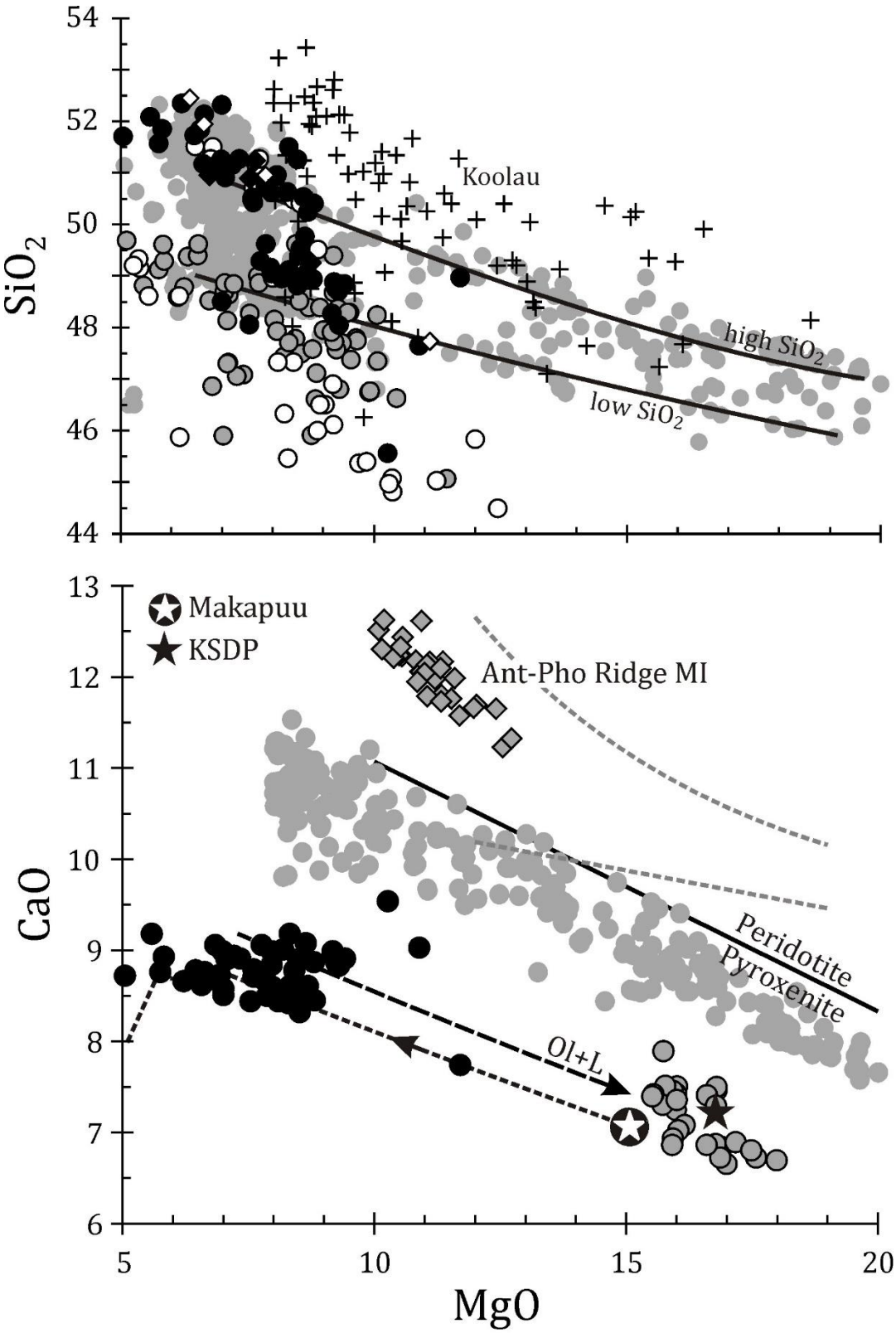
SiO2
54
52
50
48
46
44
Koolau
high SiO2
low SiO2
CaO
13
12
11
10
9
8
7
6
Makapuu
KSDP
Ant-Pho Ridge MI
Peridotite
Pyroxenite
Ol+L
5
10
15
20
MgO

Fig. 13

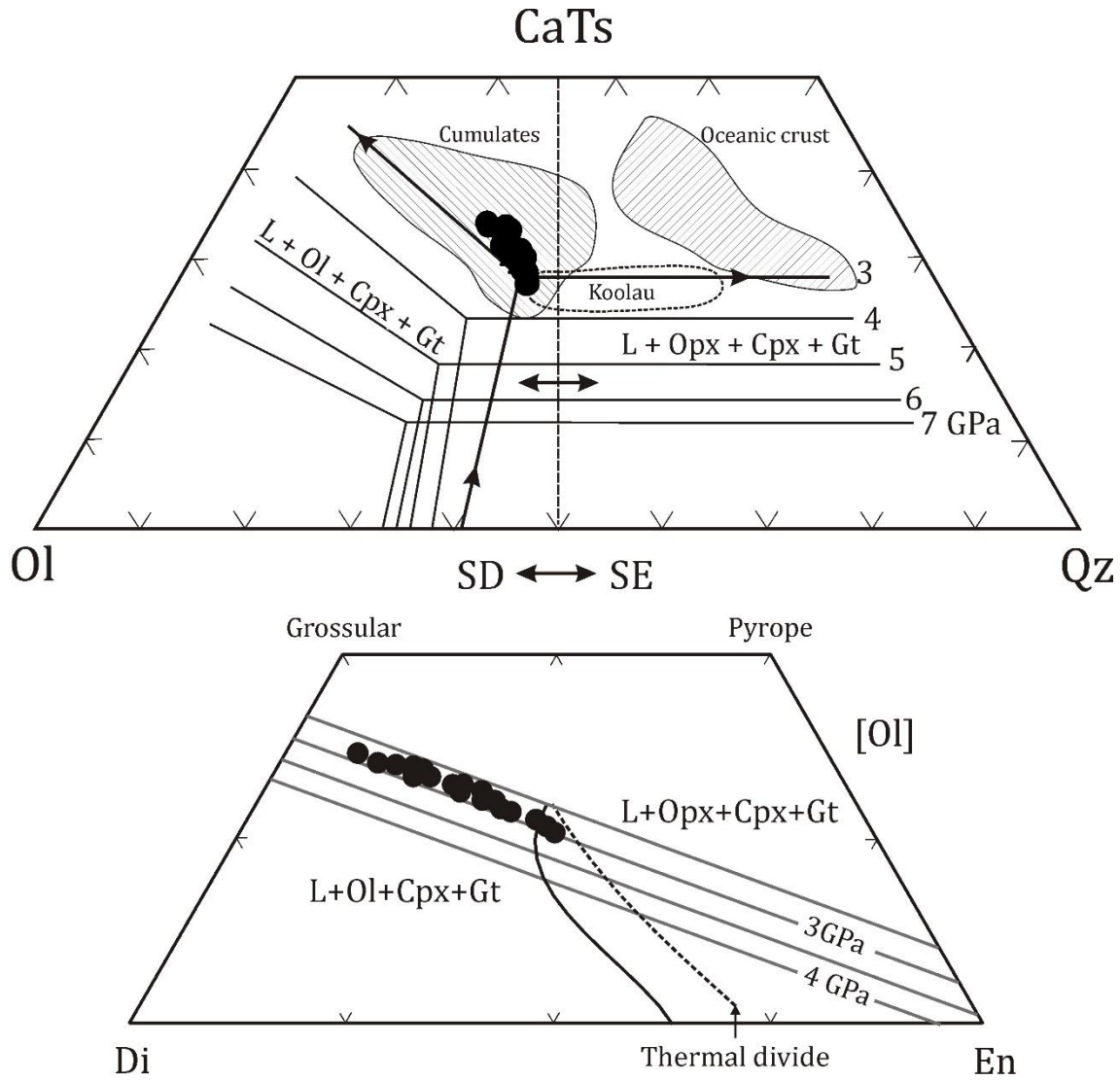
CaTs
Cumulates
Oceanic crust
L + Ol + Cpx + Gt
Koolau
3
4
L + Opx + Cpx + Gt
5
6
7 GPa
Ol
SD ⟷ SE
Qz
Grossular
Pyrope
[Ol]
L+Opx+Cpx+Gt
L+Ol+Cpx+Gt
3GPa
4 GPa
Di
Thermal divide
En

Fig. 14

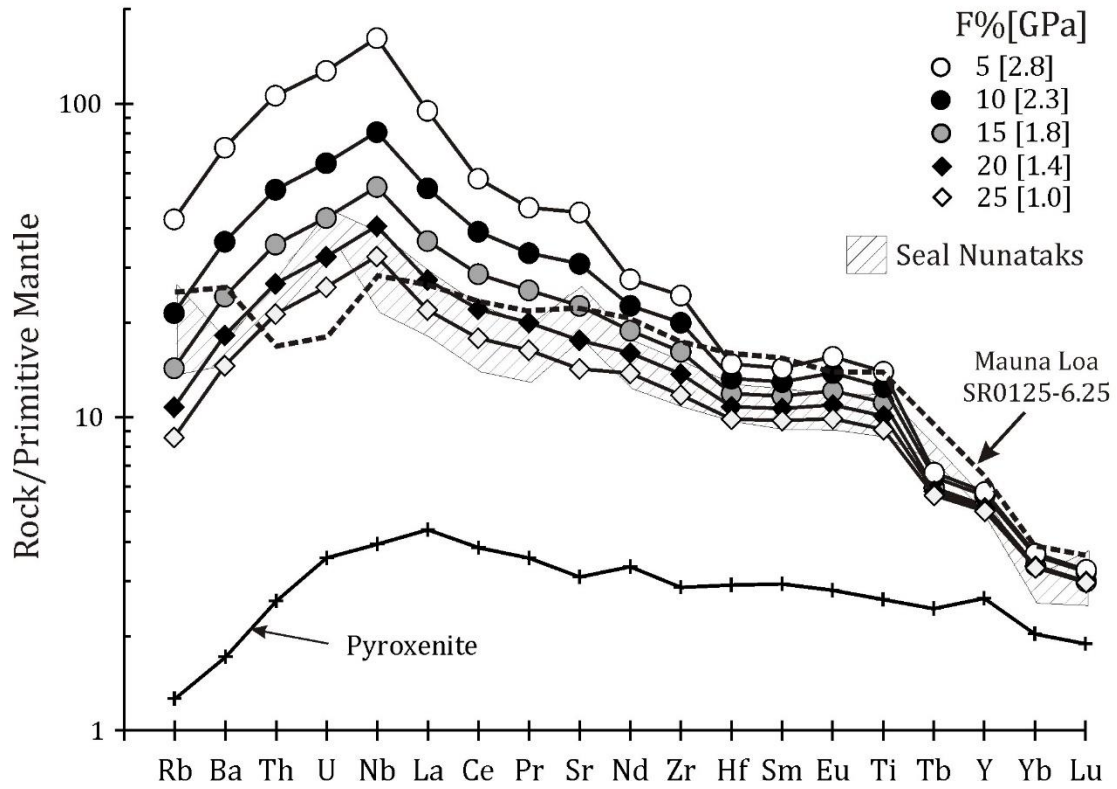
F%[GPa]
5 [2.8]
10 [2.3]
15 [1.8]
20 [1.4]
25 [1.0]
Seal Nunataks
Mauna Loa
SR0125-6.25
Pyroxenite
Rock/Primitive Mantle
100
10
1
Rb Ba Th U Nb La Ce Pr Sr Nd Zr Hf Sm Eu Ti Tb Y Yb Lu

Fig. 15

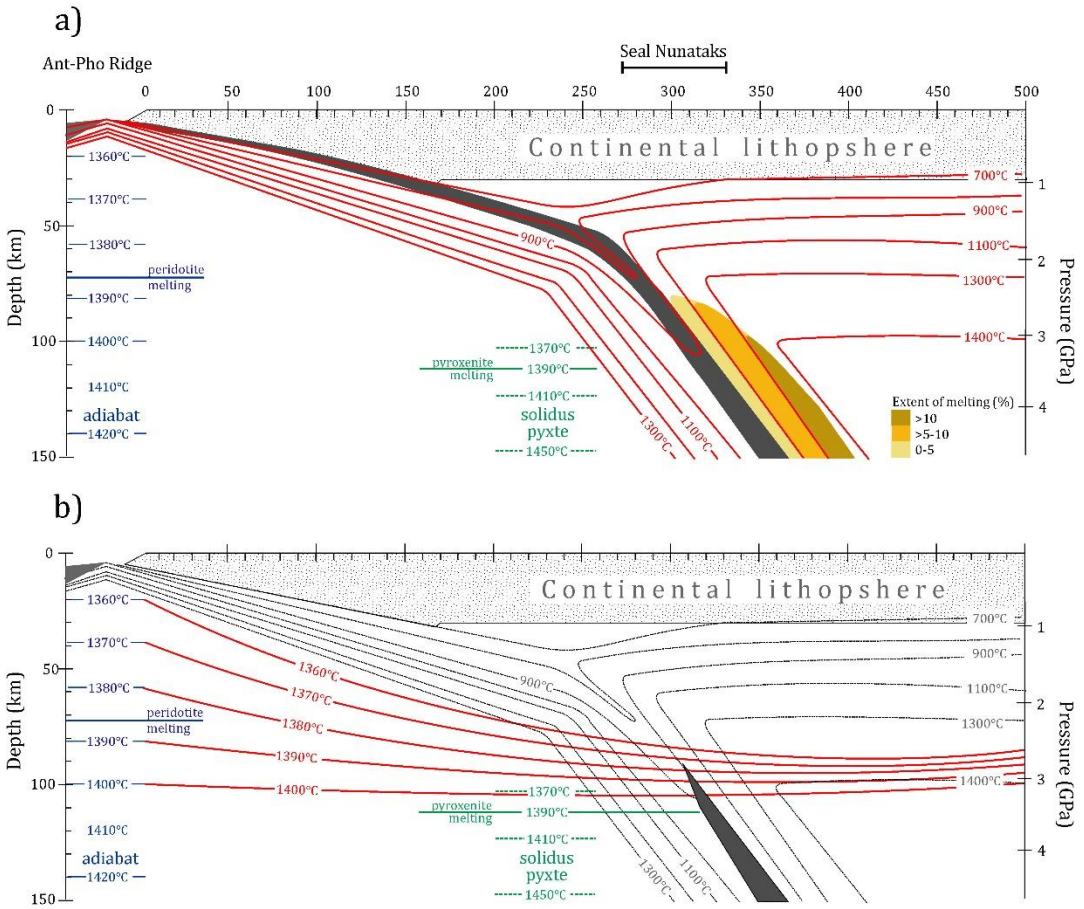
a)
Ant-Pho Ridge
Seal Nunataks
0
50
100
150
200
250
300
350
400
450
500
Continental lithopshere
Depth (km)
Pressure (GPa)
1360°C
1370°C
1380°C
peridotite melting
1390°C
1400°C
1410°C
adiabat
1420°C
700°C
900°C
1100°C
1300°C
1400°C
pyroxenite melting
1370°C
1390°C
1410°C
solidus pyxte
1450°C
Extent of melting (%)
>10
>5-10
0-5
b)
Continental lithopshere
Depth (km)
Pressure (GPa)
peridotite melting
pyroxenite melting
adiabat
solidus pyxte

Table 1. Major and trace element geochemistry of selected post-subduction basalts

Sample #	R.3728.1[1]	R.3710.9[1]	KG3625.2[2]	KG.3619.1[2]	KG.3603.5[2]	KG.3616.5[2]	D.8749.1[3]	DR.138.6[4]
SiO_2	51.50	48.93	49.51	46.90	46.11	48.60	47.78	50.95
TiO_2	1.74	2.09	1.87	2.75	2.93	2.42	1.86	1.70
Al_2O_3	14.82	14.62	14.83	14.42	14.78	16.27	14.91	17.20
Fe_2O_{3T}	9.36	11.00	10.21	8.69	9.43	9.58	10.39	7.24
MnO	0.14	0.15	0.15	0.15	0.16	0.17	0.17	0.12
MgO	8.32	8.80	8.90	9.19	9.20	6.16	8.45	7.86
CaO	8.61	8.87	8.58	10.03	8.66	7.18	8.98	8.95
Na_2O	3.34	3.45	3.29	3.88	4.25	4.67	3.34	3.68
K_2O	0.76	1.03	1.23	2.32	2.46	2.24	0.83	1.20
P_2O_5	0.24	0.33	0.36	0.85	0.77	0.83	0.34	0.21
Total	98.83	99.27	98.93	99.18	98.75	98.12	97.05	99.11
Trace elements in ppm								
Cr	346	301	326	380	187	188	257	224
Ni	132	156	152	201	152	85	123	129
Co	46.8	49.9	48.9				49.2	35.9
Rb	11	16	19	26	30	14	10	25
Sr	349	436	458	837	868	938	447	446
Ba	66	127	189	263	320	176	140	215
Hf	2.98	3.19	3.61	6.26		7.69	3.1	3.88
Zr	118	140	159	267	326	370	135	165
Nb	17	22	23	72	70	56	23	32
Ta	1.26	1.66	1.46	4.63	4.9	4	1.35	2.18
Y	21	22	24	26	25	26	24	29
Sc	21	24.3	22.9				26.6	25
U		1.05	0.86					1.01
Th	1.82	2.47	2.93	6.03	6.67	5.54	1.85	3.4
La	12.4	17.4	17.5	53.94	43.36	49.37	16.4	21.7
Ce	26.5	37.6	35	91.74	79.5	87.23	32.9	41.9
Nd	15.2	20.7	21.7	41.25	43.4	42.15	16.2	23.4
Sm	3.92	4.82	4.69	8.25	6.99	7.89	4.33	4.8
Eu	1.49	1.64	1.57	2.55	2.72	2.2	1.59	1.64
Tb	0.72	0.8	0.73	0.91	1.1	0.97		0.76
Yb	1.4	1.58	1.64	1.98	2.3	2.46	1.97	2.32
Lu	0.21	0.24	0.25	0.29	0.31	0.35	0.31	0.37

R.3728.1, alkali basalt, Evensen Nunatak, Seal Nunataks; R.3710.9, alkali basalt, Dallman Nuatak, Seal Nunataks; KG.3625.2, alkali basalt, Mussorgsky Peaks, Alexander Island; KG.3619.1, basanite, Rothschild Island; KG.3603.5, basanite, Hornpipe Heights, Alexander Island; KG.3616.5, tephrite, Mount Pinafore, Alexander Island; D.8749.1, alkali basalt, James Ross Island; DR.136.6, alkali basalt, trench proximal dredge. Data sources shown by superscript following sample number; 1. Hole (1990); 2. Hole (1988); 3. Hole et al (1994a); 4. Hole & Larter (1993).

Table 2. Calculated parental melts for slab-window related pyroxenite-derived lavas from Seal Nuntaks and Hawaiian pyroxenite parental melt compositions (Sobolev et al., 2005; Herzberg, 2006).

	Seal Nuns	HSDP-2	Seal Nuns	HSDP-2	Makapuu	KSDP
	Low SiO_2		High SiO_2			
SiO_2	47.69	47.63	49.06	48.6	51.3	50.2
TiO_2	1.72	1.85	1.49	2.04	1.5	1.5
Al_2O_3	12.23	10.54	11.91	9.94	11.3	10.8
Fe_2O_3	1.70	0.93	1.48	0.87	1.1	1.1
FeO	9.46	10.69	8.69	10.05	9.0	9.3
MnO	0.15	–	0.14	–	–	–
MgO	15.59	17.44	17.15	17.25	15.0	16.8
CaO	7.53	8.79	6.87	9.12	7.0	7.3
Na_2O	2.77	1.69	2.59	1.61	2.4	2.0
K_2O	0.88	0.28	0.72	0.29	0.4	0.3
P_2O_5	0.29	0.14	0.21	0.23	0.3	0.3
Mg#	78.5	73.6	74.8	74.6	73.8	75.4